5-2013

Exploring the Properties of Mira-Type Stars with Spectropolarimetry.

Alyssa M. Adams
East Tennessee State University

EAST TENNESSEE STATE UNIVERSITY

Exploring the Properties of Mira-Type Stars with Spectropolarimetry

by

Alyssa M. Adams

April 2013

A thesis submitted in partial fulfillment for *both*

The Honors-In-Discipline Program

&

The Midway Honors Program

in the

Department of Physics and Astronomy

College of Arts and Sciences

Richard Ignace, Faculty Mentor

Donald Luttermoser, Faculty Reader

Ariel Cintron-Arias, Faculty Reader

EAST TENNESSEE STATE UNIVERSITY

ABSTRACT

DEPARTMENT OF PHYSICS AND ASTRONOMY
COLLEGE OF ARTS AND SCIENCES

Bachelor's of Science

by Alyssa M. Adams

Mira-type stars are luminous red giants that have pulsation periods that last anywhere between 100 and 700 days. The irregular behavior of their periods and atmospheric properties flag them as excellent candidates for astrophysical studies of non-spherical stars. This paper focuses on the linear polarization of light emitted from three Mira-type stars: Mira itself, R Leo, and V CVn. Polarimetric data from the University of Wisconsin's Half-Wave Spectropolarimeter (HPOL) database, as well as other archives of polarimetric data, provide us with insight into the atmospheric and geometrical properties of these three stars. We were able to study the net polarizations and position angles alongside light curves provided by AAVSO. The observed variable polarization is a clear signature of evolving aspherical geometries for these stars. However, we found a major surprise concerning the polarimetric characteristics in V CVn, which suggest that V CVn is unlike a traditional Mira-type variable star. We end with an exploration of new possibilities regarding the atmospheric properties of V CVn.

Contents

List of Figures

List of Tables

Acknowledgements

Part of this project was funded by the National Science Foundation Research Experiences for Undergraduates (REU) program through grant NSF AST-0807664. Special thanks to the University of Wisconsin Space Astronomy Laboratory and NASA's Multimission Archive at STScI for their hard work in making data easily accessible to the public. I would also like to thank my parents and my husband for all their love and support, and a very special thanks to my advisor Dr. Richard Ignace for his dedicated mentorship throughout the entire project.

Chapter 1

Introduction

This thesis is a continuation of the paper Polarization of Light Emitted from Mira-Type Stars *published in the JSARA December 2012 issue. This paper was published to highlight the research completed within the Southeastern Association for Research in Astronomy REU supplement.*

Mira-type variable stars are cool, luminous red giants that can be found on the asymptotic giant branch (AGB) stage of stellar evolution (Willson 2005). A typical red giant can have a mass anywhere from 0.5-10 $M_{\odot}$ with an effective surface temperature that is below 5000 K (Mattei 1997). Luminous red giants, such as Mira stars, exhibit long-period variability and large pulsation amplitudes due to their late stage in stellar evolution.

After an early observation conducted in 1595, *o* Ceti was nick-named Mira (meaning "The Wonderful"), because of its brilliant 11-month luminous pulsations (Malatesta 2006). Mira became the prototype to the class of luminous pulsating variable stars, which also includes Cepheid stars and RR Lyrae stars. In general, these stars have stable and regular pulsation periods, but some luminous late-type stars exhibit irregular variability, namely, the Mira stars (Uttenthaler 2011).

Mira itself is a very popular star, and as of August 31, 1998, there have been more than 46,000 observations of Mira reported to the American Association of Variable Star Observers (AAVSO) by over 1,600 observers (AAVSO website). It is also well-known to have a nearby white dwarf companion, which, in the upper panel in Figure 1.1, is the star to the left. The images provided by the Hubble Space Telescope in Figure 1.1 reveal that Mira has an odd, asymmetrical shape that may be related to its pulsation periods (Savage 1997). This indicates that Mira is a resolved star since it is not perfectly

symmetrical. The ultraviolet image (lower right) shows Mira having a shape that differs than the shape seen in the visible light.

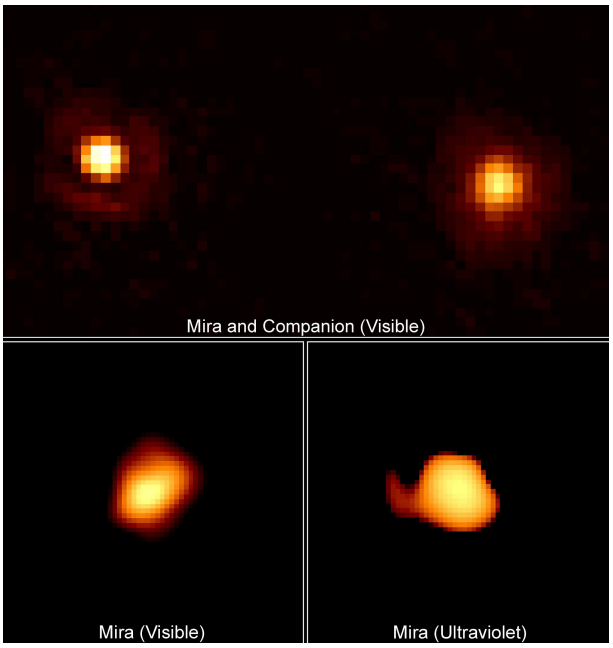

FIGURE 1.1: Images taken by the Hubble Space Telescope in 1997 of Mira and its companion (upper panel), Mira in visible light (lower left), and Mira in ultraviolet light (lower right).

Figure 1.2 shows the visual light curve for Mira, and since Mira is the prototype for Mira-type variable stars, its light curve is the prototype for Mira-type variable stars. Note that the light curve appears incomplete. The Earth's yearly orbit around the sun causes Mira's position in the sky to get too close to the Sun's position. Because the sky is brighter near the Sun, Mira's visual wavelengths cannot be observed. Also note that the vertical axis of this figure has increasing values towards the bottom, rather than the top. These values are the visual magnitudes for the brightness of an observed light source: smaller values indicate a brighter source. The values for visual magnitudes (V) follow a logarithmic scale, such that a change in brightness (ΔV) is expressed as

$$\Delta V = V - V_\circ = 2.5 \log(\frac{f_\circ}{f}) \tag{1.1}$$

where f represents the integrated energy flux in the given magnitude band. For example, a star with $V = 1$ would be 3981 times as bright as a star with $V = 10$.

In Figure 1.2, the term 'JD' refers to the Julian Date, which is an ancient unambiguous dating system that has a count of zero at noon January 1, 4713 BCE. In this thesis, we use the Modified Julian Date (MJD) which is simply 2400000.5 subtracted from the JD.

The MJD system has been the favored dating method used by astronomers since it was used in tracking Sputnik in 1957.

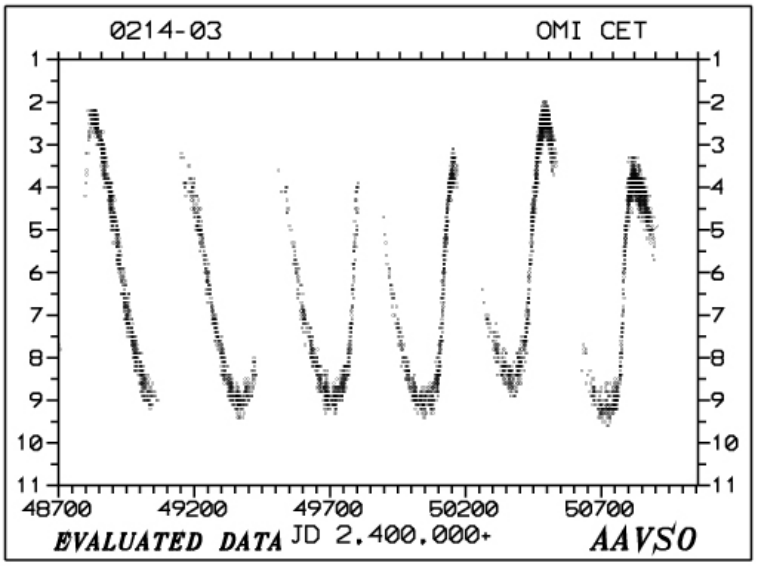

FIGURE 1.2: The visual light curve for Mira. This image was taken from the *Journal Of The AAVSO Volume 25, Number 2*, which was dedicated to the 400th anniversary of the discovery of Mira.

There are several theories which attempt to explain the mechanism that drives the pulsations of these stars. The currently favored theory suggests that pulsations are caused by the kappa effect, where kappa is the opacity factor of the stellar gas layer. A hydrogen ionization zone lies just below the photospheres of red giant variable stars. When the star is at its smallest size, the temperature peaks and the hydrogen ionizes and produces free electrons, which are opaque to all wavelengths of electromagnetic radiation. When photons move outwards from the stellar interior, they collide with these electrons and create a net momentum which pushes the free electrons, and the hydrogen layer, outwards. As this layer expands, it cools and causes the hydrogen to become neutral. As a result, the net momentum transfer and the opacity drop and the gas layers stop expanding. Gravity dominates to recover hydrostatic equilibrium and the layers shrink such that the star is at its smallest size again (Fabas, Lèbre, & Gillet 2011). The bright and dim stages of pulsating stars are caused by these opacity changes.

Our motivation for this project involves collecting data of observed net linear polarizations of light emitted by Mira-type stars to increase our understanding of their atmospheric properties. If an asymmetry exists within the star, then it will be revealed in the observation of a polarized continuum (e.g., St-Louis et.al 2011). This is attributed to a break in symmetry among the scattering particles within a circumstellar medium. A perfectly spherical distribution of these scattering particles, which in our case would indicate an unresolved source, would cancel any polarization among the circumstellar

medium and no net polarization would be observed (Vink 2011). A resolved source, then, would produce some net continuum polarization.

Although there are several Mira-type variable stars that have been observed, we chose three that are known to have been observed spectroscopically, as well as with spectropolarimetry and spectrophotometry: R-Leo, V CVn, and of course Mira, which is also referred to as *o* Ceti throughout this project. Our main source of data is taken from the University of Wisconsin Half-Wave Spectropolarimeter (HPOL) data archive. This database can be found at www.sal.wisc.edu/HPOL and the reduced polarimetric spectra are available through NASA's Multimission Archive at STScI (MAST) at archive.stsci.edu/hpol/reading.

Additional archival data collected by Serkowsi & Shawl (2001) and Poliakova (1989) contribute to our analysis of these three stars, since they feature spectropolarimetric observations during the dates preceding the observations made by HPOL. These polarimetric measurements are compared to light curve data from the well-known multi-effort Association of Variable Star Observers (AAVSO) archive.

We describe post-processing made to the HPOL data in Chapter 2 and provide an interpretation of the variable polarization in relation to an evolving source geometry in Chapter 3. Chapter 3 is also where we seek explanations for the polarization characteristics of the light emerging these stars. In Chapter 4, we assume that polarized light is caused by random bright "spots" appearing and disappearing on the surface of the star. A "toy" model was compiled in order to compare this hypothesis with the actual data. Results from several runs of the model were compiled into histograms featuring the amount of polarization and the polarization angle along with the actual mean. Final remarks and a discussion about the unique characteristics of V CVn can be found in the Chapter 5.

In addition to this this thesis, an Appendix has been added in order to supply the original and post-processed HPOL data. A short analysis of the photopolarimetric data found at MAST has also been provided in the Appendix in order to motivate future research on the photopolarimetry of Mira-type variable stars.

Chapter 2

Spectropolarimetry of Miras

The motivation behind using spectropolarimetry to study Mira-type variable stars is based on the theory that scattering particles in a circumstellar medium reveal a given amount of linear polarization, depending on the circular symmetry of the circumstellar medium (Vink 2011). Assume a star that is perfectly spherically symmetric. To a distant observer, the circumstellar medium of that star can be approximated as a flat, perfectly circular disk that is observed face-on. The light that is emitted from the disk has some measurable parameters of polarization known as the Stokes parameters.

The Stokes parameters describe linear and circular polarization, but we only consider the parameters which describe linear polarization for this project. Linear polarization has two measurement frames, q and u, which are based on equatorial coordinates. Polarization that is parallel to the North/South direction (declination) is categorized as having a positive q value, and polarization that is parallel to the East/West direction is considered to have a negative q value. The same is true for u values, with the exception that the N/S/E/W axis is rotated clockwise by 45° such that a positive u value indicates polarization in the NE/SW direction. Polarization that is equally strong in $+q$ and $-q$, or in $+u$ and $-u$ would result in zero net polarization. Thus, if there is some net polarization, then it can be immediately assumed that the circumstellar disk is not axisymmetric. Rather, it has some net geometrical deformity about its axis.

Throughout this thesis, we use linear polarization as a probe of source geometry for Mira-type stars. In particular, we are interested in three stars that have had several spectropolarimetric and spectrophotometric observations: Mira itself (also referred to as o Ceti), R Leo, and V CVn. Officially, V CVn is a semi-regular (SRa) variable star since it has a smaller amplitudes in light variability, yet in general the periods are maintained to the same extent as in the Mira stars (Luttermoser 2012). Besides this, it has several properties similar to official Mira stars that allow us to study it in the same

fashion. The interstellar medium (ISM) does play some role in our measurements, since the ISM contribution was not subtracted from the measurements. Our interest is in the *changing* polarization characteristics and long-term behavior of the stellar source, and since the ISM does not produce varying polarization characteristics, it is not necessary to subtract ISM contributions.

2.1 HPOL Data

The University of Wisconsin has produced a rich and underutilized archive of spectropolarimetric data with HPOL. The HPOL sprectropolarimeter is a modified Boller and Chivens small telescope spectrograph that provides both spectrophotmetry and spectropolarimetry in the range of 3200-10,500 Å at a spectral resolution of 10 Å. Prior to 1995, HPOL's spectral domain only went as long as 7,500 Å and at a lower spectral resolution of 25 Å. Datasets for our stars bridge across the two periods where HPOL had differing ranges and spectral resolutions. Currently, HPOL has been mounted on the 3.5 m WIYN telescope at the Kitt Peak National Observatory but will not operate fully until testing and calibration have been completed. Additional details of the instrumentation can be obtained at www.sal.wisc.edu.

The data at the HPOL website can be obtained by selecting the target data link, then selecting the object's name. A full table of spectropolarimetric data is given, with additional comments about individual readings. For example, the object *o* Ceti has a comment that says "Cloudy" for the observation MJD 48281.04. Observations with comments of this nature can be expected to yield larger errors.

Table 2.1: HPOL UBVRI synthetic filter wavelength ranges

Band	**Wavelength Range**
UX	3000Å −4200Å
B	3600Å −5600Å
V	4700Å −7000Å
R	5500Å −8600Å
I	7000Å −9200Å

HPOL uses synthetic filter polarimetry for the following wavelength ranges as given in Table 2.1. Note that UX is different than the typical U in the Johnson UBVRI passbands since it is specific to the HPOL system, thus we use UX instead of U throughout this project. Each of the letters in the Johnson UBVRI represents a specific lightband, which has a particular range in wavelength, as seen in Figure 2.1. HPOL uses synthetic filter polarimetry, which is HPOL spectropolarmetric data passed through a simulated

UBVRI filter bandpass as shown in Figure 2.1. Much information is given for each object, however we only collected data for the variables listed in Table 2.2.

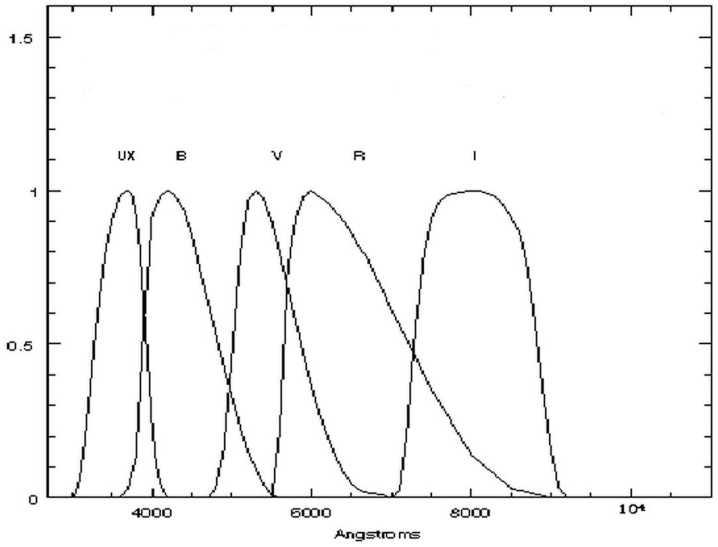

FIGURE 2.1: HPOL UVBRI Simulated Filter Bandpasses. Image taken from the HPOL website.

TABLE 2.2: Targeted HPOL data

Variable	**Detail**
$q(\%)$	Stoke's q parameter in percentage
$u(\%)$	Stoke's u parameter in percentage
$\sigma(\%)$	Percent error for data
$p(\%)$	Percent polarization
PA	Position angle of polarization

The percent polarization (p) and polarization angle (PA) relate to the Stokes parameters (q and u, which were described earlier) by means of

$$p = \sqrt{q^2 + u^2} \tag{2.1}$$

$$\tan(2PA) = \frac{u}{q}. \tag{2.2}$$

At the HPOL website, tables of broadband photopolarimetric measures can be obtained; however, only plots of the spectropolarimetry are available there. Figure 2.2 shows two of these plots as examples, one for Mira (a) and the other for V CVn (b). The pipeline reduced polarimetric spectra from HPOL are available in tabular form through NASA's Multimission Archive at STScI (MAST), which is current only to 1998 at the time of this writing. Data from 1998 to 2004 will be added in the near future.

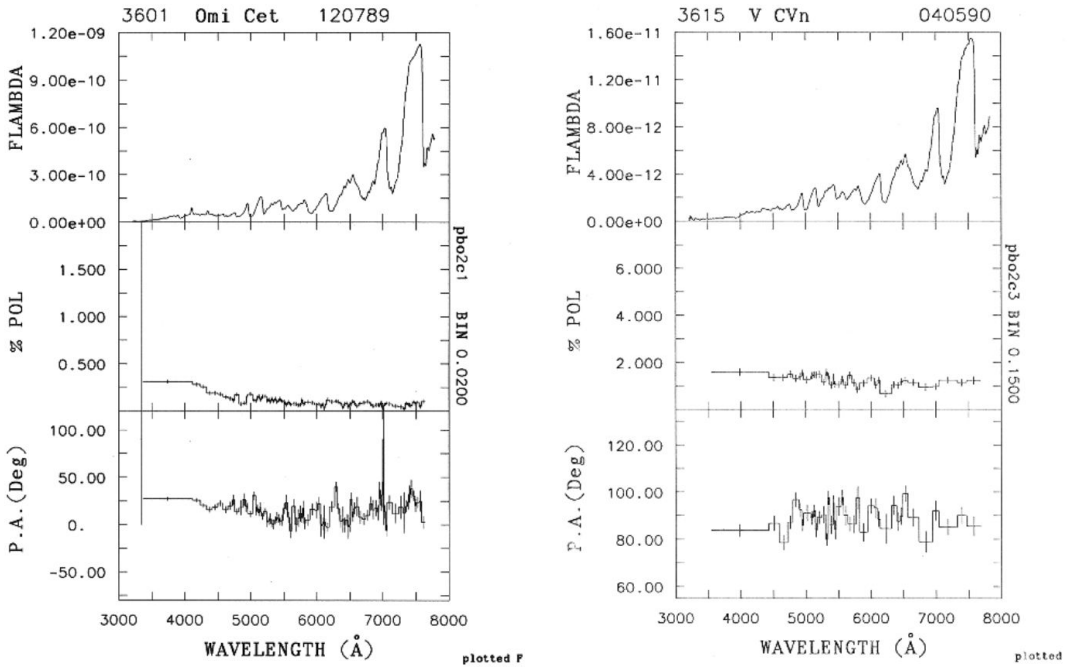

(a) *o* Ceti December 7, 1989 (b) V CVn April 5, 1990

FIGURE 2.2: HPOL spectropolarimetric data is shown for Mira and V CVn on different nights. For both (a) and (b), the top panel shows the flux with respect to wavelength, the middle panel shows the amount of polarization with respect to wavelength, and the bottom panel shows the same for the polarization position angle. Similar plots can be found for several of the 615 objects in the database.

Data for Mira, R Leo, and V CVn were obtained from MAST at www.archive.stsci.edu/hpol. Each object of interest was entered into the HPOL target data search bar, then each observation date was individually selected. The flux data were downloaded as an ASCII table.

The tabular journal of HPOL measurements (concerning Mira, R Leo, and V CVn) that was used to create the figures in this chapter can be found in Appendix A. Each table in Appendix A includes a column for each of following measurements: MJD, $q(\%)$, $u(\%)$, $\sigma(\%)$, p(%), and PA. Data in the tables are grouped according to photometric bands. We performed a cull of the datasets from HPOL. Only polarization data with detections of 3σ or higher are tabulated and used in figures, where σ is the error in the polarization measurement. In each case the fraction of data with less than 3σ (and therefore discarded) is indicated in the footnotes of each table. Most of the bad data are attributed to instances of poor quality measures, which were typically a result of bad weather or hardware issues during an observation. All of these instances can be found at the HPOL website.

2.2 Post-Reduction Processing of HPOL Data

Although the interstellar medium imposes a polarization signal on starlight, even if that starlight is completely unpolarized upon emission, the interstellar contribution is not expected to vary (e.g., Clarke 2010). Thus our focus remains on the polarization and PA changes. However, polarization position angle has a degeneracy at 180°: a PA of 180° is indistinguishable from 0°. Because we aim to identify changes in PA intrinsic to the star in order to identify changes in source geometry, it is crucial to remove artificial PA changes created by the polarization angle degeneracy as best as possible for the purposes of clarity.

Certainly, the HPOL data reveal variable PA values but they are difficult to locate. For *o* Ceti and R Leo (but not V CVn), there are a number of PA changes that are centered around 180° and 0°, with differences that amount to values at or about 180°. Such large changes are artificial, and to the eye come across as exaggerated variable polarization. In an attempt to suppress the exaggerated appearance of PA rotations that can be seen in the *original* HPOL data for *o* Ceti and R Leo, we have modified the PA values via a coordinate transformation.

Recall that the definition of the polarization position angle is

$$\tan(2PA) = \frac{u}{q} \tag{2.3}$$

and the polarization is

$$p = \sqrt{q^2 + u^2} \tag{2.4}$$

where q, u, and p are all percent values. We introduce a different reference system for the measurement of the polarized light, q' and u'. This is accomplished through a rotation matrix, called a Mueller matrix (e.g., Clarke 2010), as given by

$$q' = q\cos(2\psi) + u\sin(2\psi) \tag{2.5}$$

$$u' = -q\sin(2\psi) + u\cos(2\psi), \tag{2.6}$$

where ψ is the angle of rotation between the old reference system for q, u and the new one for q', u'. This operation ensures that the total polarization is invariant, namely

that $p = \sqrt{q^2 + u^2} = \sqrt{q'^2 + u'^2}$. But what is important is that the polarization PA is changed to PA'.

The new position angle becomes

$$\tan(2PA') = \frac{u'}{q'}. \tag{2.7}$$

Because a fair amount of the PA values for o Ceti and R Leo possess artificial jumps from 0° to 180°, we chose $\psi = 90°$ to determine the q', u' system. With this choice one can show that

$$\tan(2PA') = -\frac{q}{u} = -\cot(2PA). \tag{2.8}$$

It is PA' that is plotted in Figure 2.3 and Figure 2.4. This coordinate rotation reduced the number of artificial jumps for o Ceti in Figure 2.3, since many of the values for PA' are centered somewhere between $-50°$ and 0°. However, it remains unclear whether the coordinate transformation improved the number of artificial PA changes for R Leo in Figure 2.4 since there are still several large PA rotations.

It is true that PA changes can be viewed on a polar plot with a θ range of $0° - 180°$ rather than $0° - 360°$. This way, the degeneracy at $0°/180°$ disappears. However, it would be difficult to see how the PA changes with respect to time or polarization. Therefore, we do not include them in our analysis.

Figure 2.3, Figure 2.4, and Figure 2.5 are representations of the tabulated HPOL data along with the AAVSO visible light curves (taken from www.aavso.org/data-access) during the period 1989 to 2004. Error bars (σ values) are given for each point, which are all reasonably small. Some error bars are not visible, simply because the point is larger than the length of the error bars. The top panel of Figure 2.3 shows the HPOL PA' values in degrees for the UX (yellow), V (cyan), B (blue), R (red), and I (green) bands for o Ceti. Values for PA' are plotted in degrees against date in MJD. Again, it is important to note that PA' differs from PA. The visual light curves from the AAVSO are shown in the bottom panel. Figure 2.4 shows data for R Leo in the same manner as the previous figure.

The top panel for Figure 2.5 shows PA values for V CVn, not PA', since no coordinate rotation was applied. Because the majority of the AAVSO light curve observations was

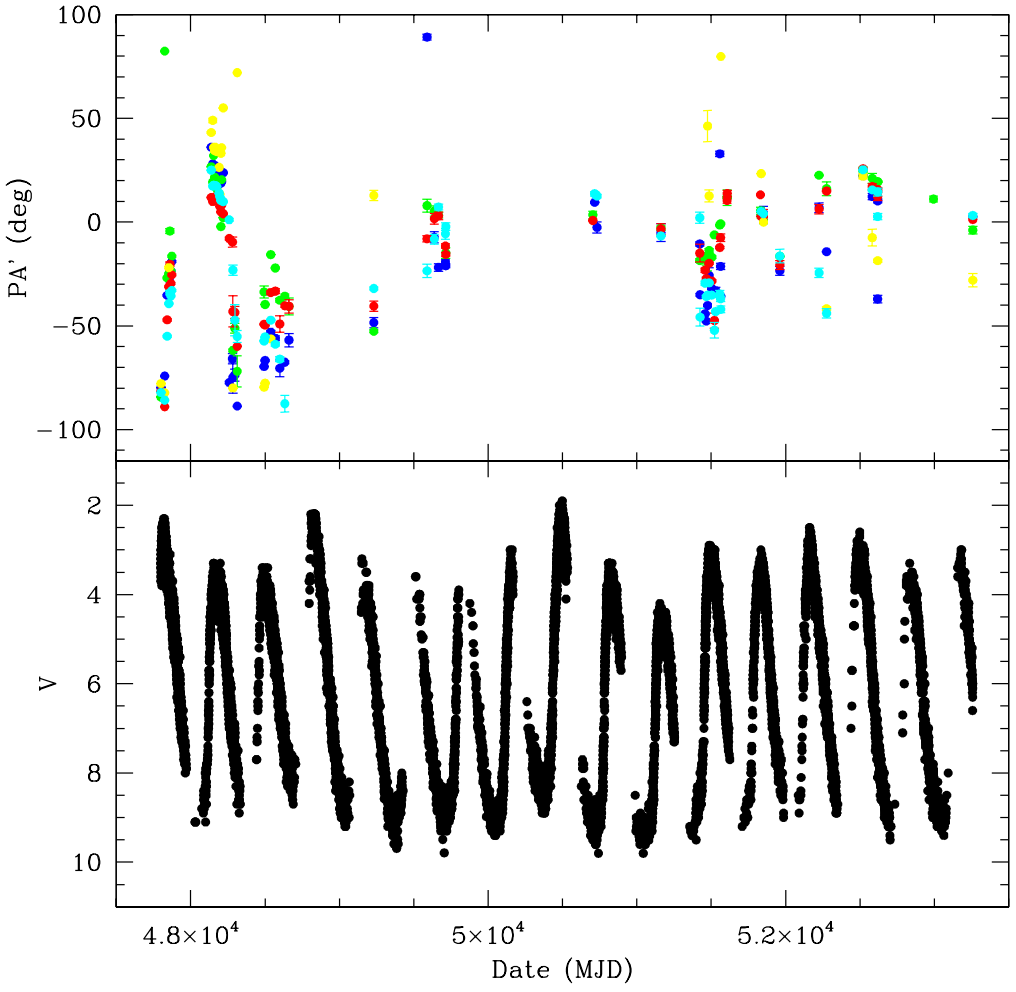

FIGURE 2.3: *o* Ceti. Top: HPOL spectropolarimetry data for PA' in degrees with UX (yellow), V (cyan), B (blue), R (red), and I (green) bands. Bottom: AAVSO visual light curves.

performed by a single observer, most of the values for the visual magnitude have been rounded in the same fashion (to only two significant digits), thus giving the light curve a noncontinuous appearance. The points have therefore been connected for clarity.

It is important to note that polarimetric data that are compared against the light curve are generally within the light curve maxima– when the star appears the brightest. This is typical for these types of measurements because polarization tends to be low for stellar sources, at the level of 0.1%–1% typically, and thus requires bright sources to achieve good quality measures of the polarization level.

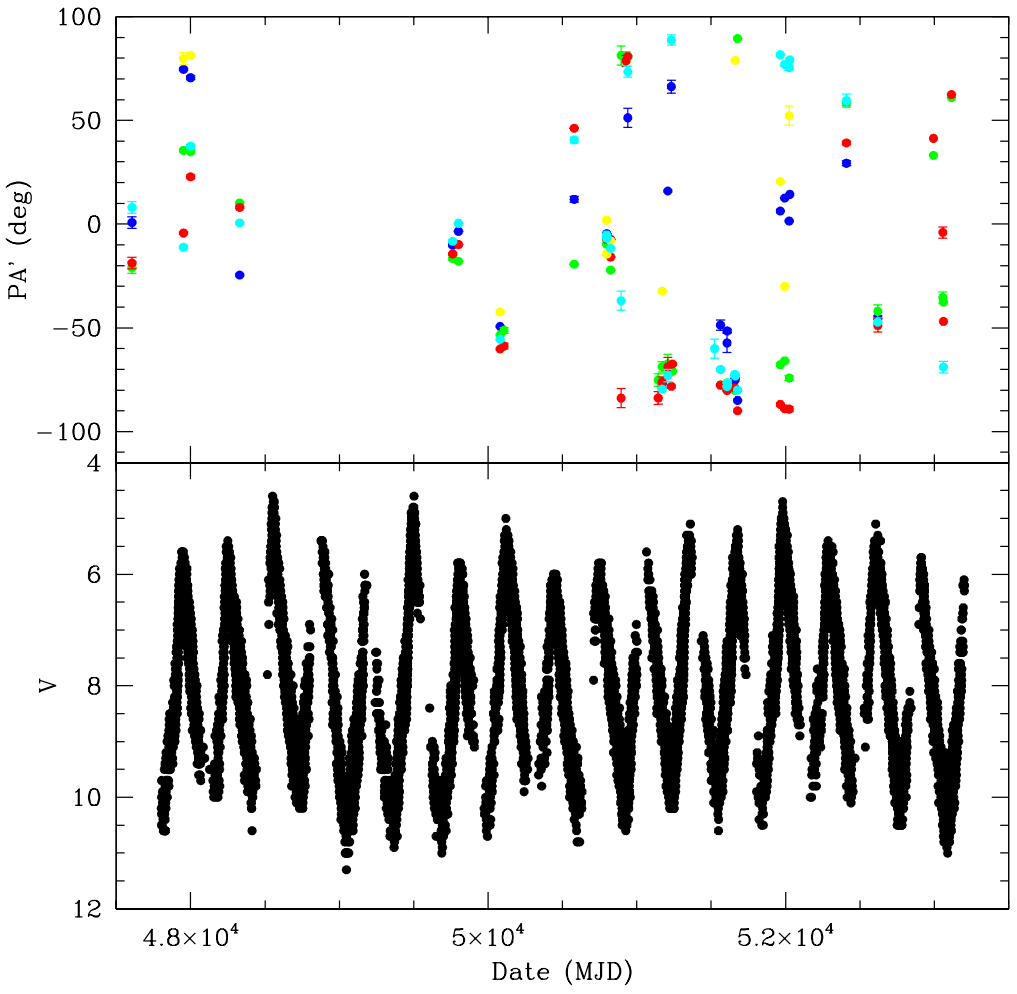

FIGURE 2.4: R Leo. Top: HPOL spectropolarimetry data for PA' in degrees with UX (yellow), V (cyan), B (blue), R (red), and I (green) bands. Bottom: AAVSO visual light curves.

2.3 HPOL Individual lightband Data

For closer analysis of the polarimetric data in each individual lightband, Figure 2.6, Figure 2.7, and Figure 2.8 have been provided. Each figure contains two subfigures. The subfigures on the left are representative of the time evolution of percent polarization, while the subfigures on the right represent the time evolution for position angles. Note that none of these three figures include PA', but only include PA. Error bars are not included in these figures as well. In general, the polarimetric data are more sparse in the UX band, due to the lack of significant data. It is significantly more difficult to

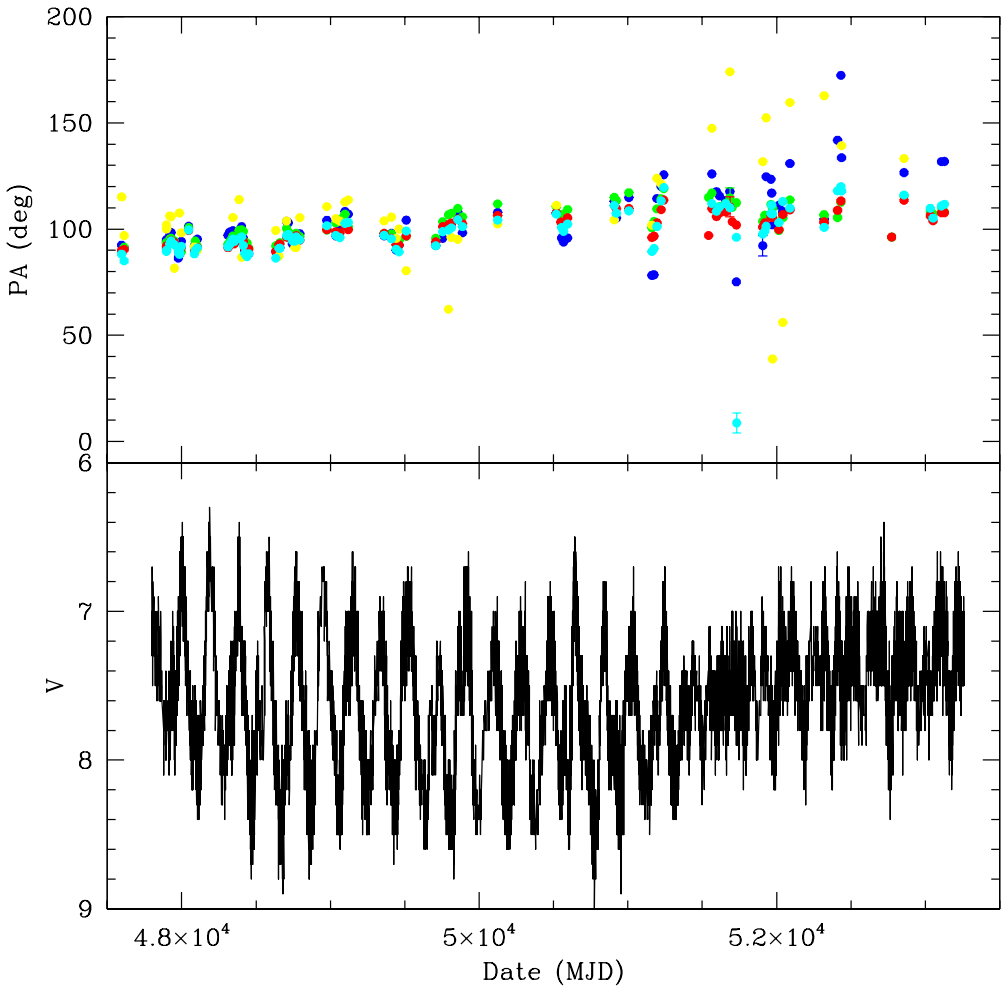

FIGURE 2.5: V CVn. Top: HPOL spectropolarimetry data for PA' in degrees with UX (yellow), V (cyan), B (blue), R (red), and I (green) bands. Bottom: AAVSO visual light curves.

record data from a source beneath the Earth's atmosphere in this wavelength, and as a result, the data are flagged with several comments on the HPOL website regarding the difficulty.

Figure 2.6 shows these data for *o* Ceti. This star exhibits dramatic PA changes, especially between MJD 48000 and 50000. However, it is difficult to tell which PA changes are intrinsic to the star and which are due a degeneracy. The polarization also exhibits variability. R Leo (Figure 2.7) has the same features regarding PA and polarization variability, however R Leo has a wider range for polarization. In general, the polarization values increase as the wavelength decreases, yet does not lose its amount of variability.

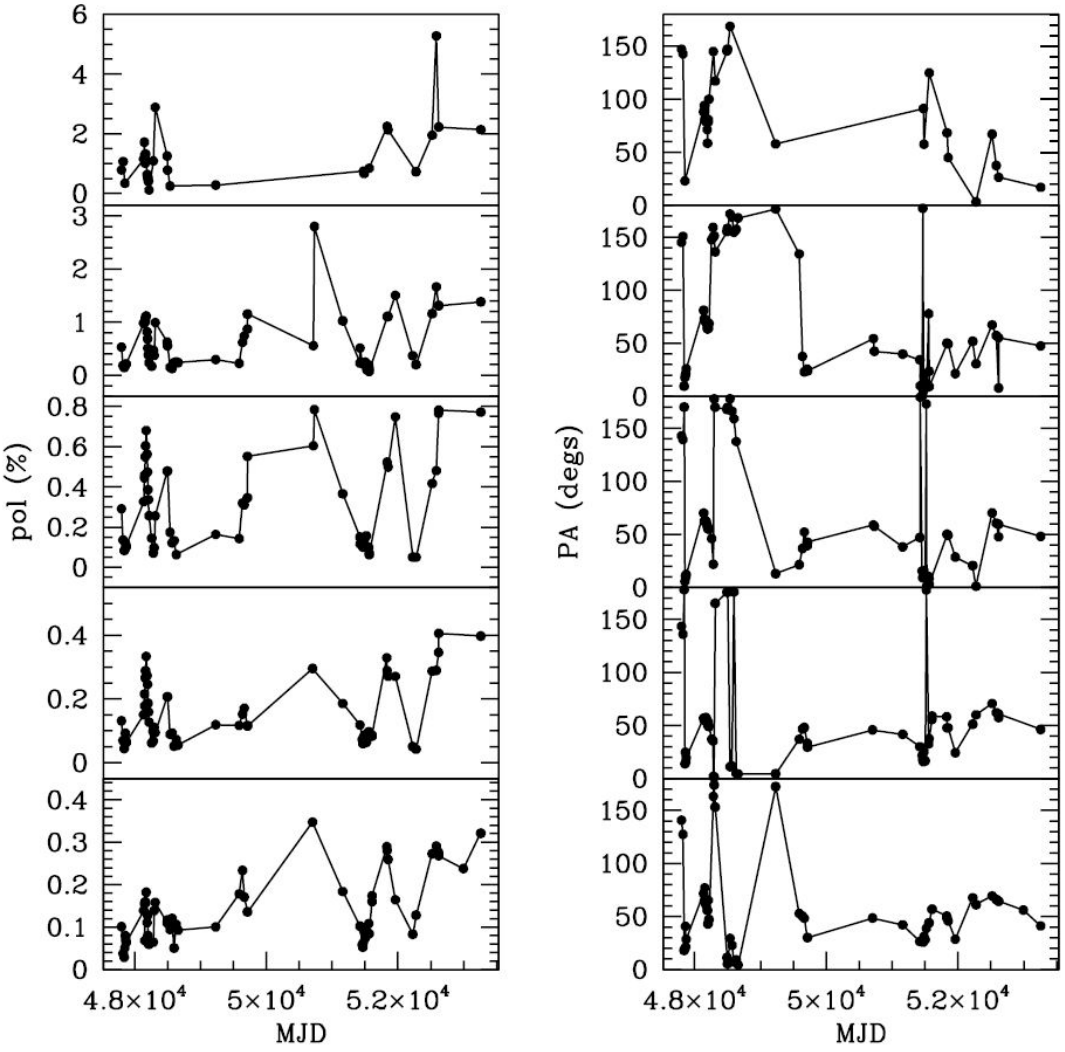

FIGURE 2.6: HPOL Polarimetric data for *o* Ceti. From top to bottom, each panel represents a corresponding lightband: UX, V, B, R, and I, respectively.

Out of these three figures (Figure 2.6, Figure 2.7, and Figure 2.8), it is obvious that there is a star that is not like the other two. V CVn does not exhibit the same PA and polarization variability as *o* Ceti and R Leo. In fact, its values for PA remain fairly constant until MJD 51000. PA variability also increases as wavelength decreases. For V CVn, PA values in the UX band are significantly more variable than the PA values in the I band and values for polarization almost seem periodic in every lightband. Unlike the other two stars, there is a semi-regular period for polarization. We take a closer look at V CVn's uniqueness in contrast to the typical Mira pulsating star later in Chapter 5.

With such large variations in the PA values, it is difficult to determine the effect of the ISM, but Figure 2.9(a) and Figure 2.9(b) indicate that most of the PA changes are intrinsic to the star itself. These two figures indicate that the amount of polarization is not highly favored for any particular polarization angle. Figure 2.9(a) indicates that the light emitted by *o* Ceti has its highest values of polarization when the PA is at

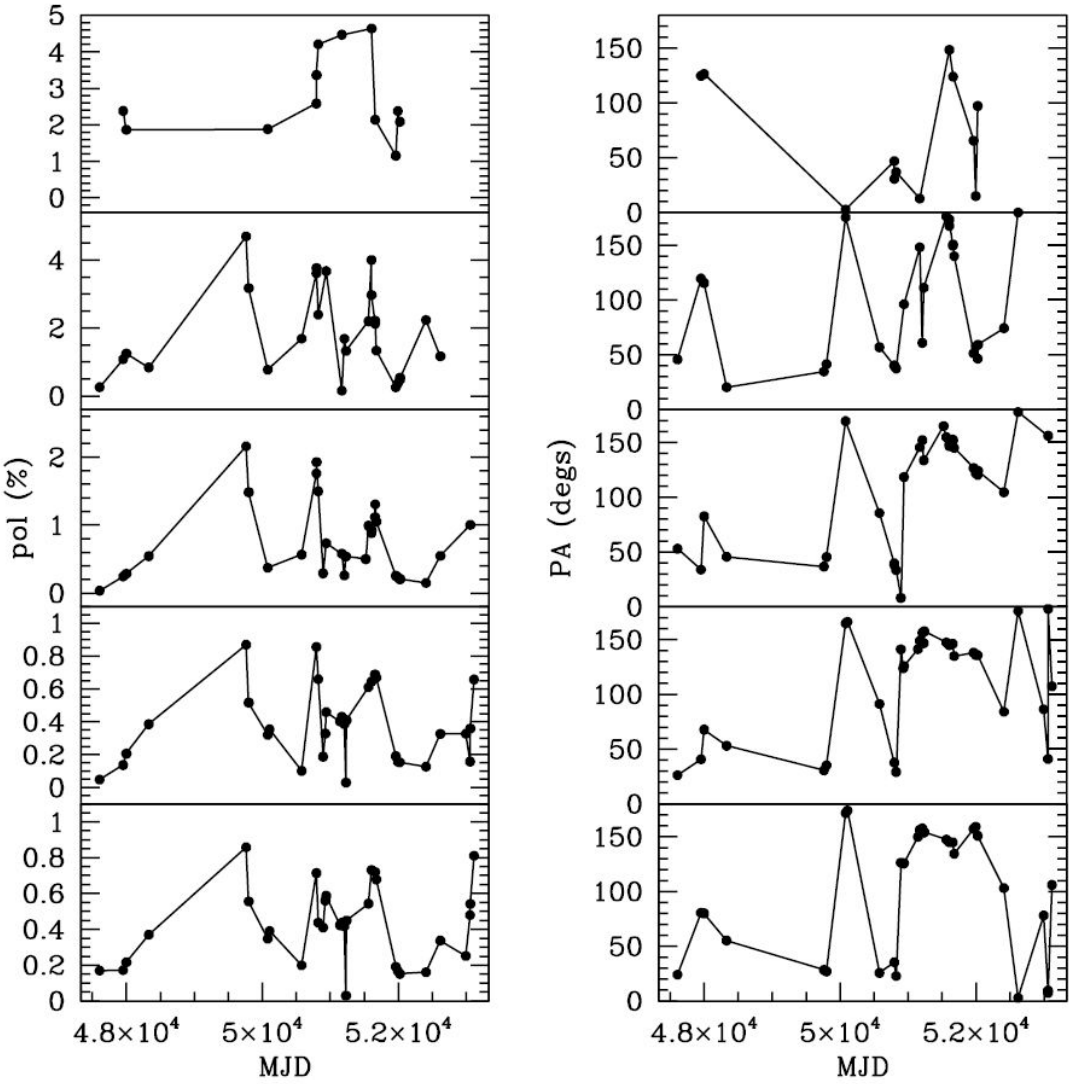

FIGURE 2.7: HPOL Polarimetric data for R Leo. From top to bottom, each panel represents a corresponding lightband: UX, V, B, R, and I, respectively.

about $10° - 70°$. Because the distribution for polarization is not narrow around these PA values, the range of values for PA are intrinsic to the star itself, not the ISM.

In general, R Leo exhibits slightly higher values for polarization than *o* Ceti, but with greater variance. Its PAs are also highly variable as well, which made the rotation fix (discussed in Section 2.2) difficult to perform. The highest values for polarization occurs near a PA of 150 degrees, which again could indicate contributions from the ISM. The other amount of polarization near a PA of 45 degrees is most likely intrinsic to the star.

Figure 2.9(c) shows that V CVn has a fairly regular distribution of polarization values at around 100°. We know that V CVn is a Mira-type variable star, yet this figure alone does not indicate that the star pulsates, since one might be able to argue that most of the polarization is attributed to the ISM. However, this is not the case. Upon examining

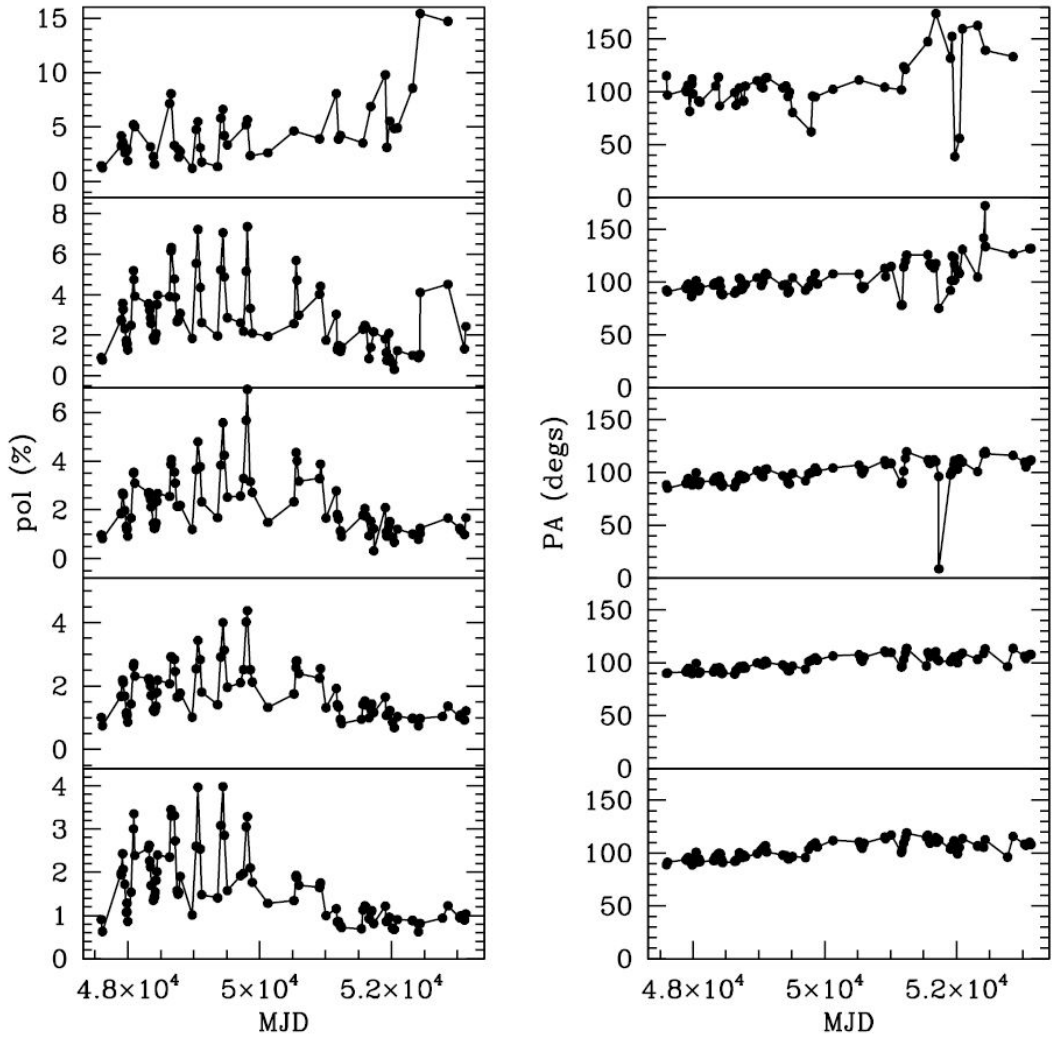

FIGURE 2.8: HPOL Polarimetric data for V CVn. From top to bottom, each panel represents a corresponding lightband: UX, V, B, R, and I, respectively.

Figure 2.5, we see that the PA values are fairly consistent before MJD 51000, but then lose their consistency and exhibit variability after MJD 51000. This feature is even more fascinating when compared to V CVn's AAVSO light curve: note how the light curve changes around MJD 51000 as well. The light curve indicates a semi-periodic pulsation behavior, with unique polarization and PA characteristics with respect to the other two stars. These features will be discussed in Chapter 3 and in Chapter 5.

2.4 Archived Data

Besides HPOL, there were two other rich data sets that feature spectropolarimetric data for *o* Ceti, R Leo, and V CVn. Serkowski & Shawl compiled a very large collection of spectropolarimetric data for 167 different cool variable stars, including RV Tauri stars

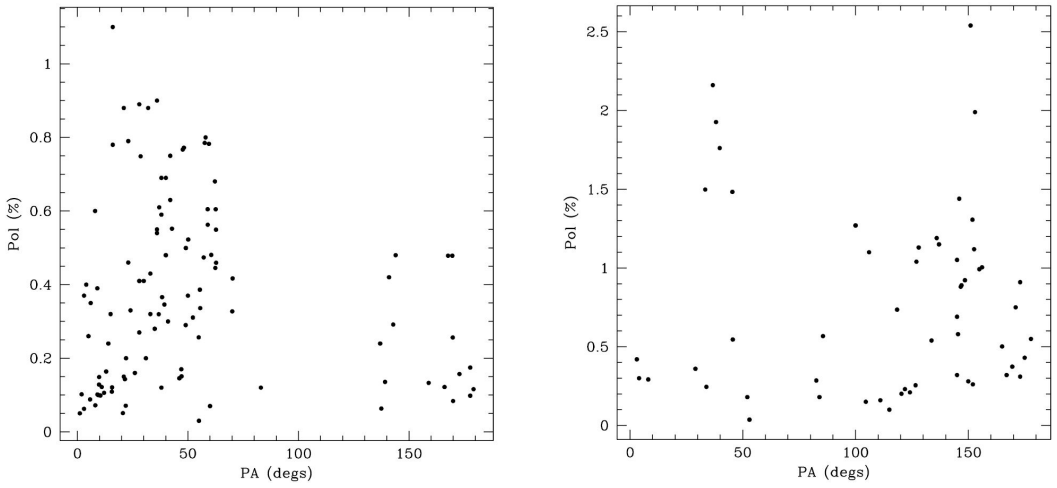

(a) *o* Ceti

(b) R Leo

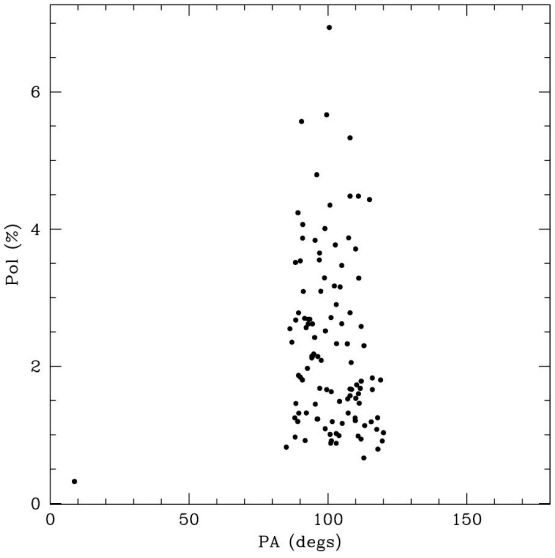

(c) V CVn

FIGURE 2.9: Pol(%) vs. PA for *o* Ceti (a), R Leo (b), and V CVn (c).

and classical and Population II Cepheids. These multicolor data cover observations from 1966 to the late 1970's, which is a time span of about 15 years, along with a few additional observations in the spring of 2001. The data supplies values for both the amount of polarization and its position angle, such that the polarizing environments in and around these cool stars may be understood (Serkowski & Shawl 2001).

Most of the broadband polarimetric observations of red variable stars were collected by Serkowsi from several publications in the 1970's. The observations were done using a few different telescopes, such as the telescope at the Lowell Observatory in the UBV spectral regions, the Siding Springs telescope in the UBVR photometric bands, and the Lunar and Planetary Laboratory telescope in the UBV photometric bands. For additional details regarding the data and instrumentation, see Serkowski & Shawl (2001). Poliakova

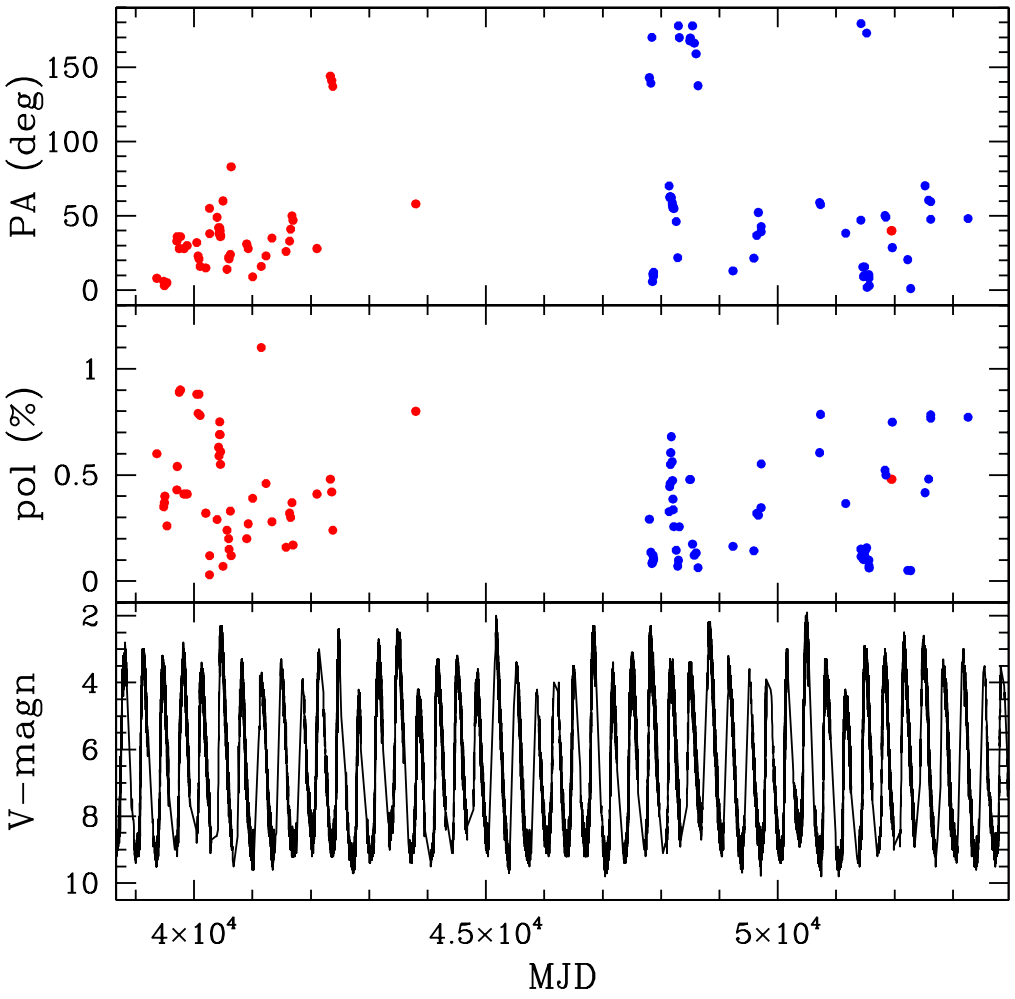

FIGURE 2.10: Data provided by Serkowski & Shawl (red) and HPOL (blue) for *o* Ceti (top) is shown alongside the corresponding AAVSO light curve (bottom).

published the results of polarization observations for the star V CVn in 1989. These observations include PA and polarization values for the B band and V band during the years 1980−1986.

Figure 2.10, Figure 2.11, and Figure 2.12 feature the spectropolarimetric data collected by Serkowski & Shawl (shown as red points) together with the V band data from HPOL (shown as blue points), along with the light curve from the AAVSO for our three stars of interest. The purpose of adding these datasets with the HPOL data is to confirm the long-term polarimetric behavior of these stars. All three of these plots indicate that HPOL's data and the previous data are consistent with each other, which is valuable for

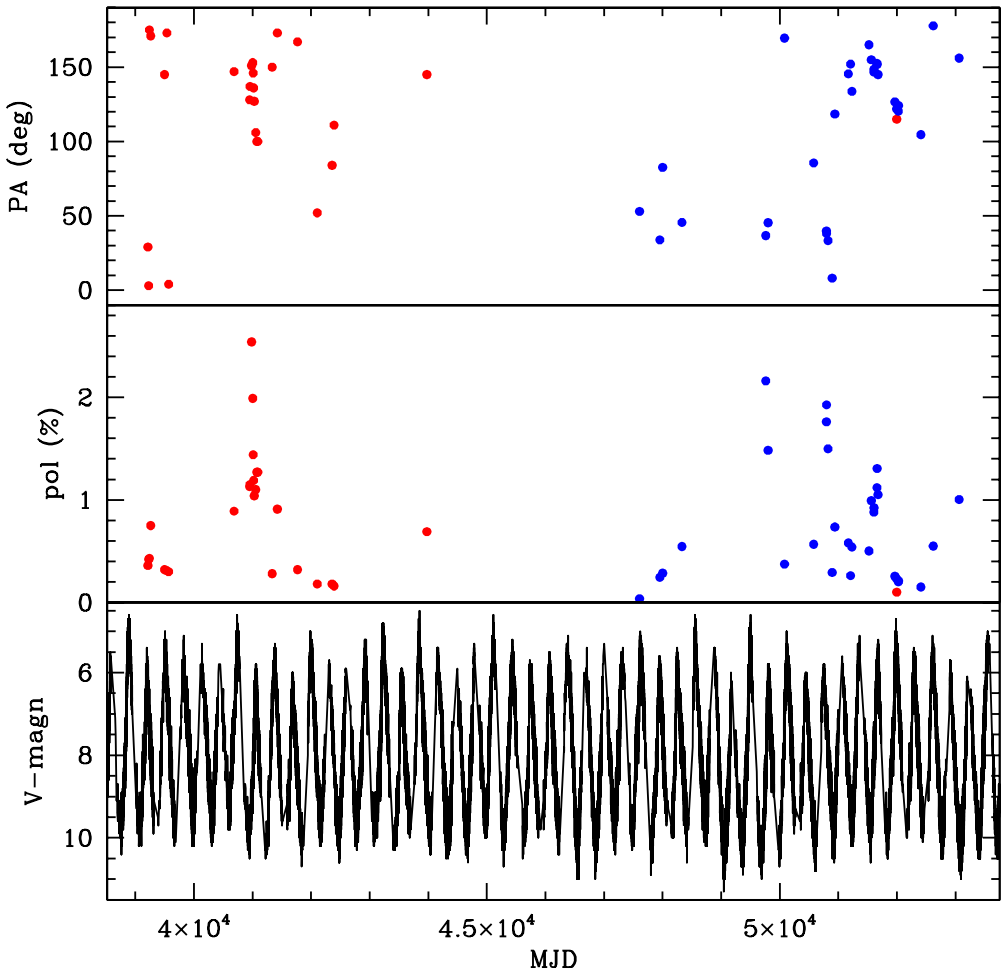

FIGURE 2.11: Data provided by Serkowski & Shawl (red) and HPOL (blue) for R Leo (top) is shown alongside the corresponding AAVSO light curve (bottom).

understanding the atmospheres of these stars.

Notice the HPOL values for polarization for V CVn in Figure 2.12 and all the polarization values in Figure 2.13. The values for HPOL in Figure 2.12 have an envelope of maxima that peaks around MJD 50000. The B band values of polarization in Figure 2.13 display the same feature that peaks around the same MJD. Figure 2.13 also suggests the presence of two other envelopes of maxima, one which peaks at MJD 45000 and another that peaks around MJD 39000. A lack of data prevents a visible repeating pattern of such polarization behavior, but there *is* one such envelope in both the V band and B band with a peak at MJD 50000.

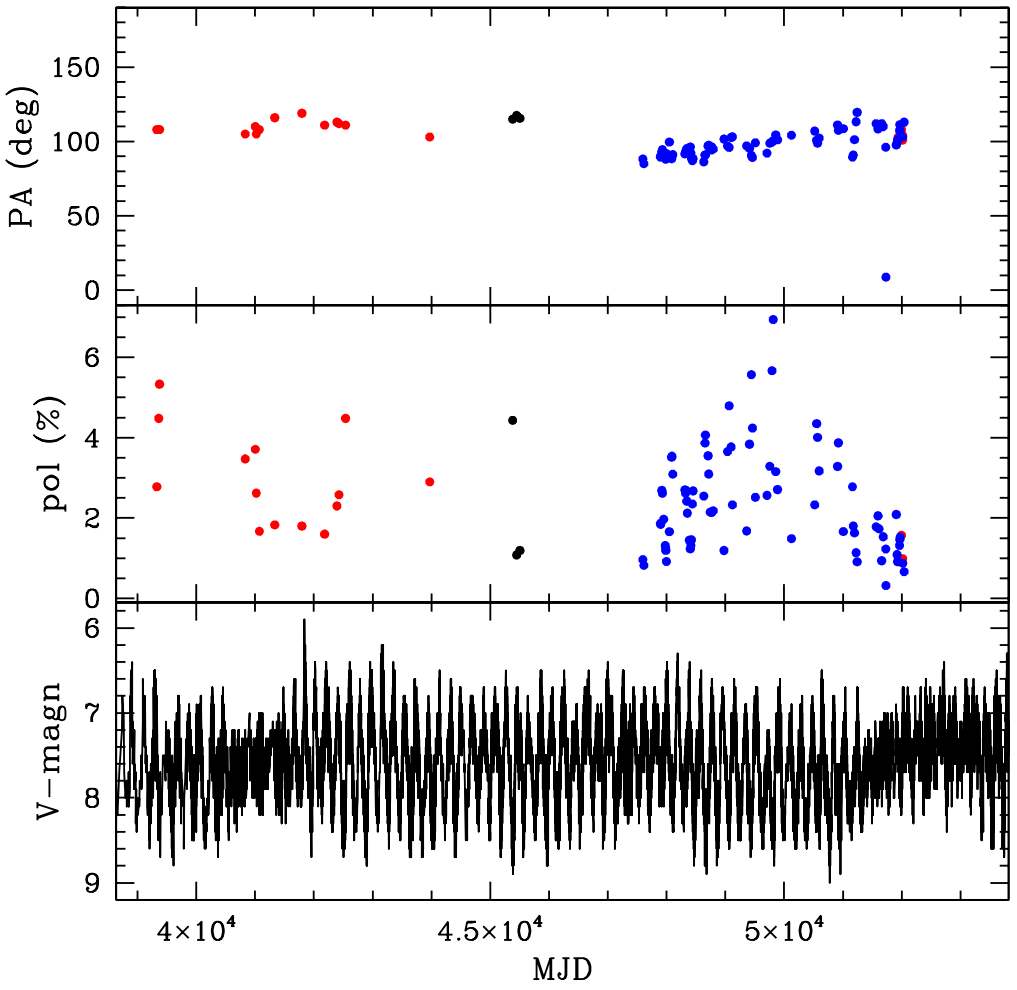

FIGURE 2.12: Data provided by Serkowski & Shawl (red) and HPOL (blue) for V CVn (top) is shown alongside the corresponding AAVSO light curve (bottom).

Also note the AAVSO light curve (bottom panel) at MJD 51000. Before this date (and after MJD 42000), the light curve has identifiable pulsation periods. After MJD 51000, the pulsation periods become ambiguous and semi-regular. The same feature in V CVn's light curve can be found near MJD 41000. These areas in the light curve are of particular interest because they suggest the presence of additional factors within the atmosphere of V CVn. It would be helpful to see a repeating trend during the times that V CVn's light curve loses its periodicity, however the current data lacks enough observations to detect any repeating trends.

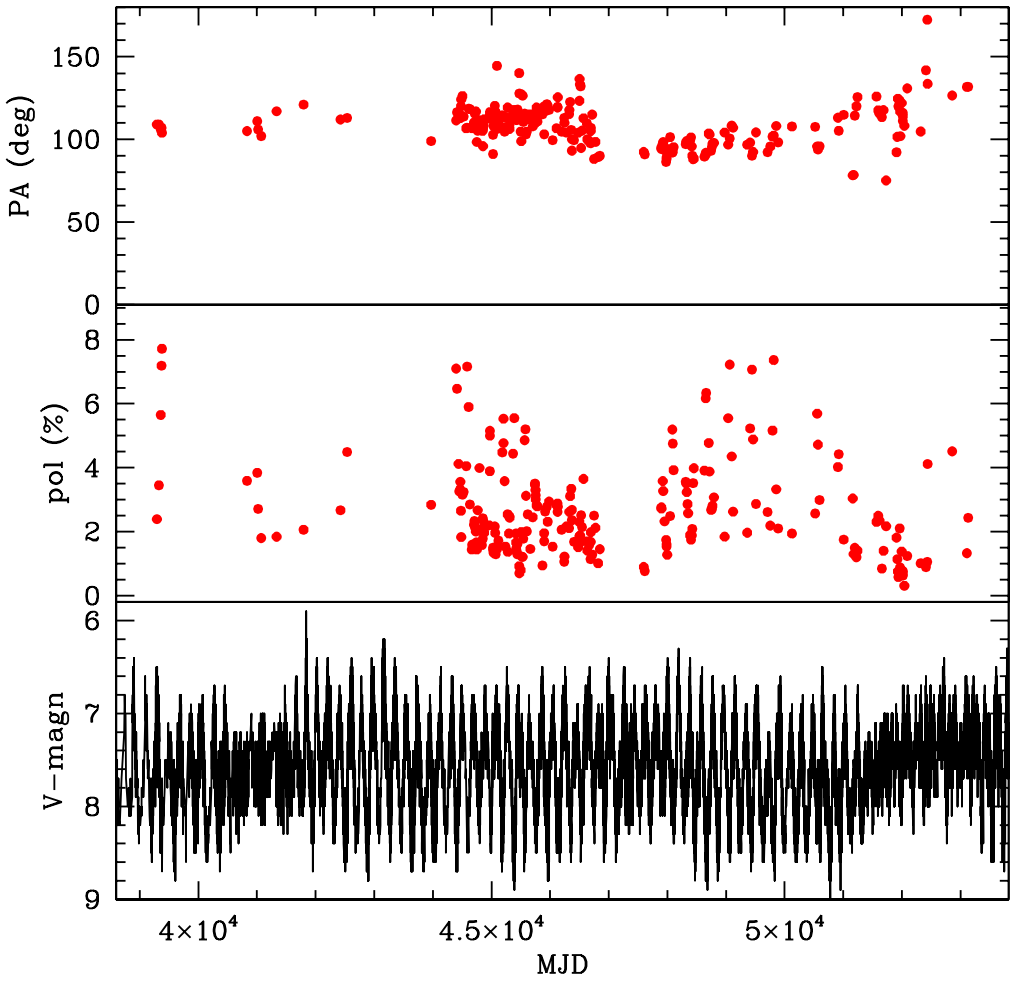

FIGURE 2.13: Polarimetric observations of V CVn in the B band provided by Poliakova (top) is shown alongside V CVn's corresponding AAVSO light curve (bottom).

Chapter 3

Interpretation of the Data

As stated in the previous chapters, the purpose of the observations made by Wisconsin's HPOL, Serkowski & Shawl, and Poliakova is to increase our understanding of the polarizing environments in and around these cool red variable stars. Specifically, we aim to consider the values of the PA, which reflects the asymmetry of a star in an orientation with respect to the observer's North, and the amount of polarization. In order for a net polarization to be observed from an unresolved star, that star must have non-spherical characteristics (Raveendran 2002). Knowing this, it follows that a change in PA is the result of a change in the star's asymmetry and asymmetry orientation. Rotations of PA are likely caused by variable geometry in a region of spectral formation.

3.1 The PA Changes

While examining the figures in Chapter 2, we witness remarkable and rapid PA rotations in each of the five lightbands for *o* Ceti and R Leo. However, we do not observe this in V CVn. Here, we mean "rapid" to be a minimum of a 10° PA rotation between observations about a week apart (which constitutes about 2% of the star's average pulsation period). PA rotations are particularly erratic in the UX Band for both *o* Ceti and R Leo, which is likely due to the presence of larger errors in the measurements. Unlike *o* Ceti and R Leo, the PA in each lightband for V CVn is fairly constant before MJD 51000. This indicates the presence of a fairly stable geometry with respect to time. However, the sudden PA rotations are fascinating to witness, especially since they occur near times when the AAVSO light curve changes its pulsation period behavior.

The differences in PAs at maximum light have been noted by Hayes & Russo (1981) for *o* Ceti. In *o* Ceti, nonspherical pulsations, grain growth in the extended atmosphere, or

changes in convective cells in the lower atmosphere may play a role in these PA changes (Hayes & Russo 1981).

We assume that the unstable and unpredictable nature of the PA is a consequence of a similar, complex atmospheric geometry in R Leo. The future promises fascinating insights if the stellar atmospheres of these stars were to be modeled. In Chapter 4, we explore the possibility that these changes in PA may be a result of the coming and going of spots in the stellar atmosphere, rather than a changing non-spherical source geometry. We use this model for Mira and R Leo, but not V CVn, since the distinct characteristics of V CVn suggest that this star cannot be modeled in the same fashion. Thus, we do not attempt to model the PA characteristics for V CVn in this thesis, yet a model for V CVn would be an excellent topic for future research.

3.2 Statistical Analysis

So that we may understand what is causing the polarization of light in these stars, we consider the time-averaged polarization with respect to the wavelength in Figure 3.1. One curve is shown per star plotted on a logscale, resulting in three reasonably straight lines. The linear regression of polarization versus λ appears for each star as a dotted line such that their slopes can be easily obtained, as listed in Table 3.1. There are three types of scattering mechanisms that are found in cool stars. Electron scattering is constant at all wavelengths (and frequencies) of the electromagnetic spectrum. This causes free electrons in the atmosphere to be very opaque to any wavelength. Mie scattering is independent of wavelength across the infrared and visual bands, and largely depends on the size of scattering dust particles. Both Mie and electron scattering would produce a curve with zero slope in Figure 3.1. But because these curves *do* have non-zero slopes, we can consider the third scattering mechanism. Since the Rayleigh scattering law of polarized light emitted from a source has a wavelength dependence of λ^{-4} (Clarke 2010), the equation for each of the dotted lines can be described as

$$\log p = m \log \lambda + b \tag{3.1}$$

where p is the time-averaged polarization, m is the slope of the line, and λ is the wavelength. On a non-logarithmic scale, these same curves would be described by negative exponential values. The exponent is represented as λ, which is the same value for the slopes in Figure 3.1. It is easy to see that polarization increases as wavelength decreases, which is evidence of the Rayleigh scattering found in previous studies (Harrington 1969;

Yudin & Evans 2002). Since electron scattering would produce curves with zero slope, it is safe to assume that Rayleigh scattering is more favored in these these atmospheres. However, perfect Rayleigh scattering would produce slopes that are equal to -4, and since none of the values in Table 3.1 are equal to -4, we do not observe ubiquitous Rayleigh scattering.

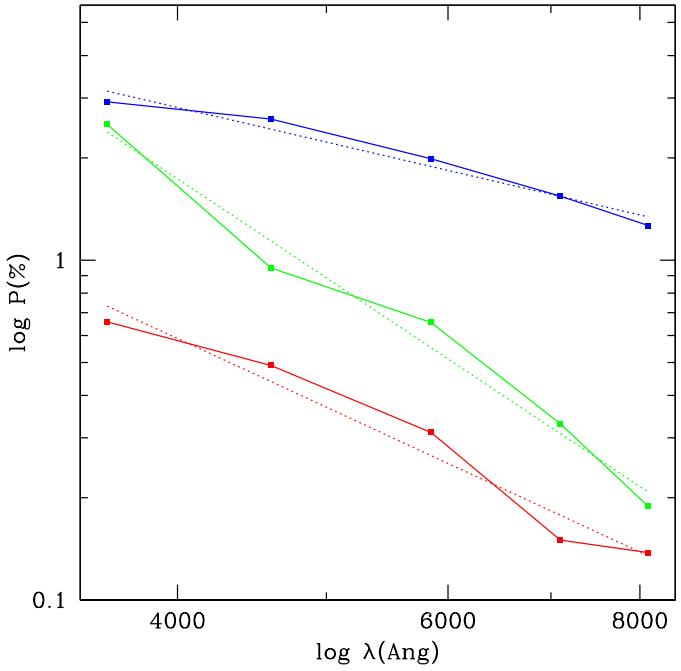

FIGURE 3.1: Wavelength (Å) vs. Average P(%). Each point represents the time-averaged polarization in one of the five lightbands on the HPOL bandpass filters. The red curve is representative of *o* Ceti, the green curve is representative of R Leo, and the blue curve is representative of V CVn.

TABLE 3.1: m values from Figure 3.1.

Star	m
Mira	-2.09
R Leo	-3.01
V CVn	-1.05

On average, Mira variable stars display larger values for polarization than what a classical model predicts, which is most likely caused by temperature variations, stellar spots, or convection cells on the stellar surface (Harrington 1969). For Mira and V CVn, the polarization increases when hydrogen emission lines become visible (Shawl 2001) which indicates a large number of small particles being produced with each pulsation period. This is consistent with our previous knowledge concerning these types of stars. This

evidence is further supported by Yudin & Evans (2002), who suggest that polarimetric variability that is more evident in the blue rather than the red is evidence of episodic mass ejections along with the formation of small dust particles within the circumstellar environment.

Dyck (1968) conducted polarimetry and photometry for 21 late-type Mira stars and found a correlation between polarization and brightness. In general, an increase in brightness yielded a decrease in polarization. Dyck also noted the same increase in polarization in the blue, just as we see in Figure 3.1.

We can turn away from spectropolarimetry and into narrow-band filter measurements in order to identify the source of polarized light within the stellar atmosphere. In general, it was found that most post-asymptotic giant branch (AGB) stars exhibit some intrinsic polarization, with most of the polarization effects appearing more commonly in the O-rich bands (Beiging, Schmidt, Smith et al. 2006). Mira was monitored at maximum light by McLean & Coyne (1978). This study found a large amount of Balmer emission lines along with decreases in polarization within the TiO bands. Tomaszewski, Landstreet, McLean et al. (1980) confirmed this observation and suggest that the polarization as a function of λ is a result of scattering in an atmosphere that is not uniformly bright.

Measurements made by Magalhaes, Coyne & Benedetti (1986) on V CVn indicate that absorptions in the TiO band reinforce the idea that most polarization occurs within the photosphere, along with an intermediate scattering layer in the stellar atmosphere. They confirm the model of a pulsating molecular scattering atmosphere which links polarization to the pulsation cycle. Changes within the TiO band are caused by changes in the absorption-to-scattering ratio with respect to optical depth. This is further evidence of a photospheric origin for most optical polarization, along with the presence of an intermediate scattering layer within the stellar atmosphere.

3.3 Incidence of Polarization Values

It is useful to examine the incidence of the PA and polarization values in each star. Using all three datasets (HPOL, Serkowski & Shawl, and Polikova), the following histograms were created. We use our modified values for position angle (PA') instead of the raw PA values from the HPOL dataset for Mira and R Leo. There are four histograms shown for each of our three stars: two of the histograms show the incidence of the PA and polarization values in the B band, while the other two histograms show the incidence of the PA and polarization in the V band.

Figure 3.2 and Figure 3.3 reveal that most of the PAs in Mira occur between 0° to 70°. The interstellar medium was *not* taken into consideration. Since the ISM contributes a constant value for PA and polarization, a varying PA and polarization indicates a change that is intrinsic to the source. So it is easy to see that Mira and R Leo are exhibiting geometrical variability. The large variations in PA values in Figure 3.4 and Figure 3.5 indicate that most of the PA changes are intrinsic to R Leo.

Once again, it is easy to see the difference between V CVn and the other two stars. V CVn does not have such a large variation in its values for PA in both the B band and the V band. Also, the polarization values in the V band are higher than the polarization values for R Leo and Mira.

We also show the polarization and PA values with respect to V-magnitude for Mira and V CVn in Figure 3.8. R Leo is not shown in the figure since it is very similar to Mira. There is no clear trend in polarization values or in PA values with respect to V-magnitude in Mira. The values for PA are not the values for PA' as discussed previously. V CVn has polarization values that tend to increase when the star appears dimmer, which is unlike Mira and R Leo. The PA values are constant with respect to the star's brightness.

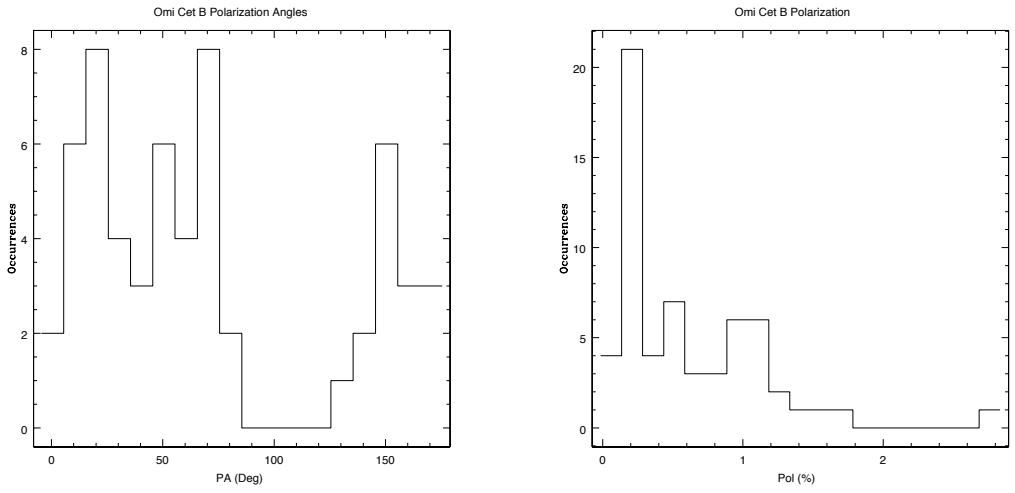

(a) *o* Ceti B band polarization angles

(b) *o* Ceti B band polarization (%)

FIGURE 3.2: The incidence of PA (a) and polarization (b) in the B band for *o* is given.

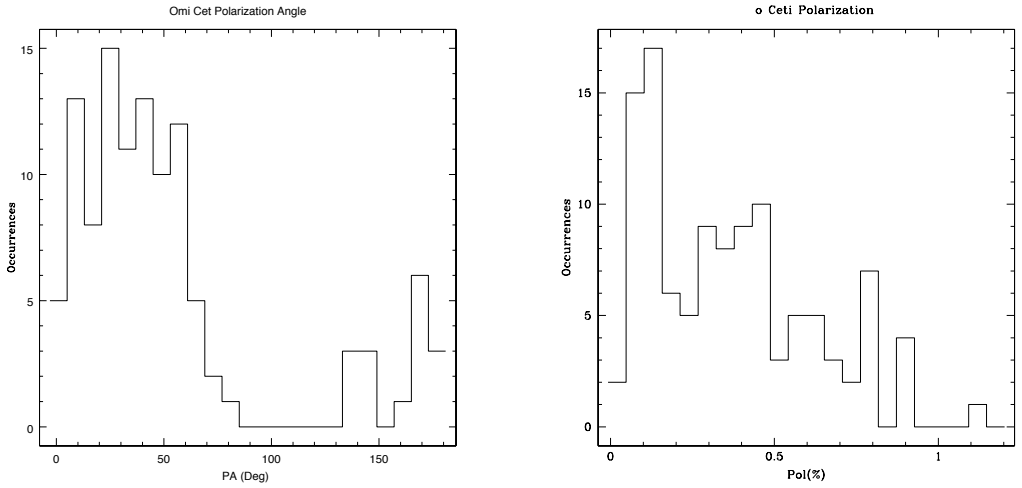

(a) *o* Ceti V PA (b) *o* Ceti V p(%)

FIGURE 3.3: The incidence of PA (a) and polarization (b) in the V band for *o* is shown.

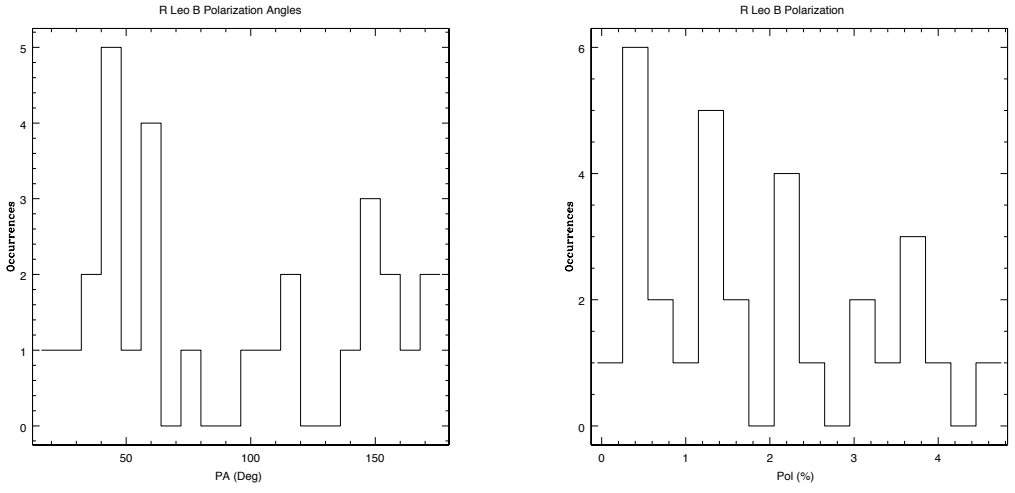

(a) R Leo B band polarization angles (b) R Leo B band polarization (%)

FIGURE 3.4: The incidence of PA (a) and polarization (b) in the B band for R Leo is given.

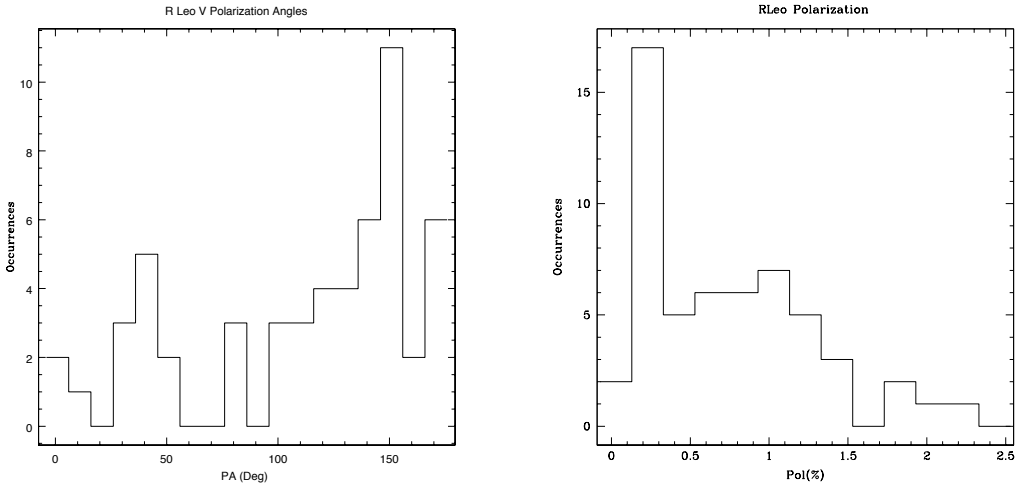

(a) R Leo V band polarization angles

(b) R Leo V band polarization (%)

FIGURE 3.5: The incidence of PA (a) and polarization (b) in the V band for R Leo is given.

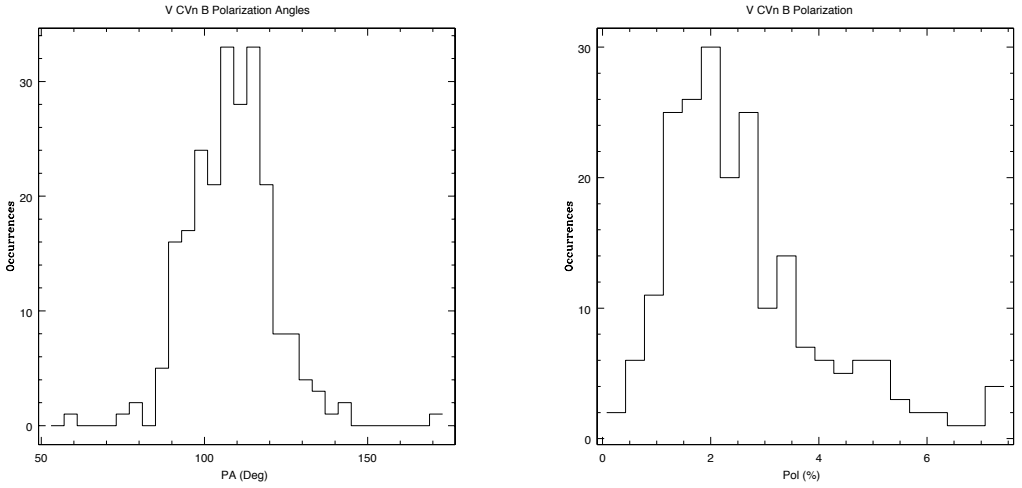

(a) V CVn B band polarization angles

(b) V CVn B band polarization (%)

FIGURE 3.6: The incidence of PA (a) and polarization (b) in the B band for V CVn is shown.

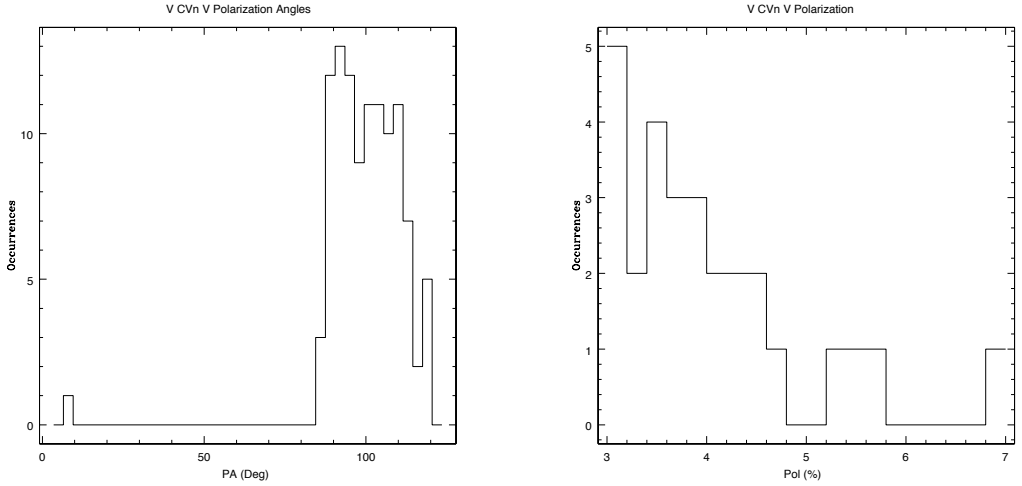

(a) V CVn V band polarization angles

(b) V CVn Vband polarization (%)

FIGURE 3.7: The incidence of PA (a) and polarization (b) in the V band for V CVn is given.

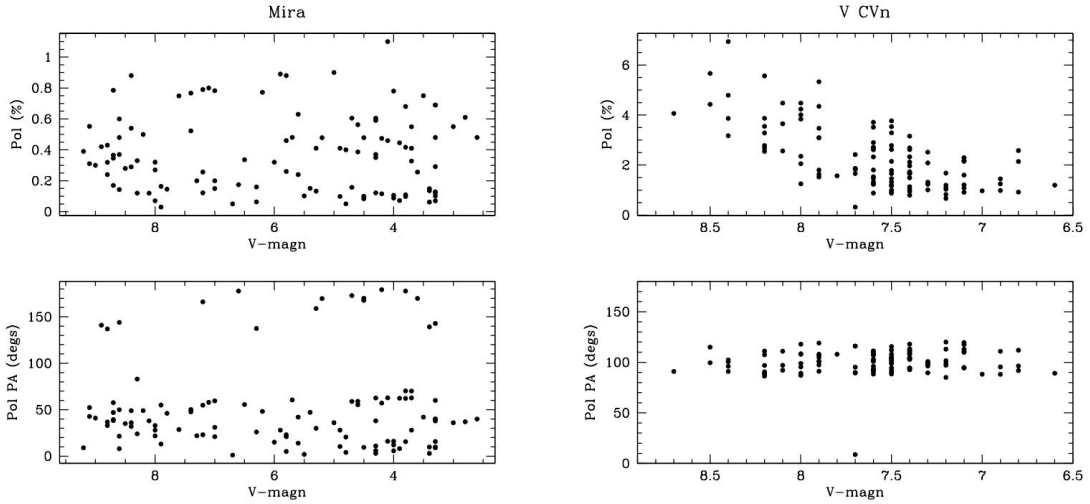

FIGURE 3.8: Values for polarization (top panels) and PA (bottom panels) are shown with respect to the V-magnitude for Mira and V CVn. R Leo is not shown since it is similar to Mira.

Chapter 4

A Starspot Model and Results

In an attempt to understand how R Leo and *o* Ceti have such a wide range of values for polarization and PA, we invented a 'toy' model in the spirit of linking our basic knowledge of polarimetry to our observations. We know that the Sun has regions on its photosphere that vary in brightness due to the physical properties of the Sun's atmosphere. The areas on the Sun's surface that are brighter are due to the presence of convection cells, granulae, and faculae.

We hypothesize that Mira and R Leo have similar, visibly bright regions in their photospheres, and these spots are responsible for our observed highly variable PA and polarization values. Although Mira stars are not at the same stage of stellar evolution as the Sun, Tomaszewski, Landstreet, McLean et al. (1980) suggest that the polarization of light in Miras is a result of scattering in an atmosphere that is not uniformly bright. Therefore it is safe to hypothesize that Mira stars may have bright regions within their atmosphere.

In this discussion, these regions areas are called 'spots', but it should be emphasized that the term 'spot' does not refer to dark areas in the photosphere, as does the term 'sunspot' when used in context with our Sun. Our model 'spots' are circular regions that are bright with respect to the rest of the stellar surface, but are not assumed to be associated with any particular atmospheric phenomenon. These 'spots' are simply, and nothing more than, bright spots.

Brown and McLean (1977) assert that whenever we consider a spherical star and an axisymmetrical envelope, the dipole scattering polarization (p) of light that is emitted is

$$p = \bar{\tau}(1 - 3\gamma)\sin^2(i). \tag{4.1}$$

Here, $\bar{\tau}$ is the average optical depth, which always has a value that is less than a factor of 1 for our model photospheres. If we assume that the layers where the polarization occurs is optically thin, then we assume that $\bar{\tau}$ is less than 1. In our model, we are only concerned with the bright (optically thin) stages of Mira and R Leo, such that the atmospheres are not considered to be opaque. The shape factor for the object in question is described with γ. Consider a perfect sphere. Its shape factor must be equal to 1/3 since no net polarization would be observed from a perfectly spherical source of light, assuming the distribution of scattering particles is uniform within the circumstellar envelope (Vink 2011). The angle of inclination, i, is defined as $i = 0$ when an observer is pole-on and equator-on with the observed object. The relation $p \propto \sin^2 i$, in conjunction with the definitions of p and PA, define the basis for our model.

4.1 Model Description

For purposes of simplicity, our model star is axisymmetric such that the stellar illumination is axisymmetric. Therefore, it follows that any bright, stationary spot on the stellar surface would result in non-isotropic illumination that would yield a value of polarization (p) and a value for that polarization's position angle (PA). No polarization would result from geometrical deviations from a perfect sphere. Since $\tan(2PA) = u/q$ and $p = \sqrt{q^2 + u^2}$, the Stokes parameters for linearly polarized light would be defined as

$$q = p\cos(2PA) \tag{4.2}$$

$$u = p\sin(2PA) \tag{4.3}$$

With respect to the center of the star, we assume a single spot to have a longitude of θ and a latitude of ϕ. The summation of multiple (N many) spots would then result in a net linear polarization with the Stokes parameters

$$q_{total} = \sum_{i=1}^{N} p_i \cos(2PA_i) \tag{4.4}$$

$$u_{total} = \sum_{i=1}^{N} p_i \sin(2PA_i) \tag{4.5}$$

where the total polarization of the system (p_{total}) is

$$p_{total} = \sqrt{q_{total}^2 + u_{total}^2}. \tag{4.6}$$

Within the model, spots are randomly generated in time and in location on the surface of the star. These spots are assumed to be small enough such that no spot is partially occulted with respect to the observer. In comparison to the photosphere, the spots are given an excess brightness whose brightness contribution follows a Gaussian profile. The summation of spots that exist simultaneously can result in more polarized light if the spots' parameters do not cancel in their summation.

There are a number of factors within our model that will manipulate the outcome of polarization. Table 4.1 describes these parameters, which is a description of variables that can change within our model star.

TABLE 4.1: Optional variable parameters for the model

Parameter	**Purpose**
τ	Spot lifetime
s	Spot seeding rate
N	light curve duration
d	Spot temperature enhancement
m	Star luminocity power exponent
n	Star temperature exponent

A pulsating star has luminocity L that varys with time t and can be characterized with an exponent value m:

$$L = L_\circ[1 + a\cos(\omega t)]^m, \tag{4.7}$$

where $L_\circ$ is the initial value for luminocity, a is a constant, and ω is π divided by the pulsation period. Using the same notation, the temperature T of a pulsating star can also characterized by an exponent value n:

$$T = T_\circ[1 + b\cos(\omega t + \phi)]^n. \tag{4.8}$$

The additional variable ϕ is simply the phase shift that separates the peaks of L from the peaks of T. Because Mira stars pulsate, their radius R changes as a function of time. We use

$$L = 4\pi R^2 \sigma T^4, \tag{4.9}$$

which assumes the model is a blackbody where the energy flux is given by the Stefan-Boltzmann law of blackbody radiations. Since L and T both vary with time, we see that

$$R = \sqrt{\frac{L(t)}{4\pi\sigma T^4}} \propto \frac{[1 + a\cos(\omega t)]^{m/2}}{[1 + b\cos(\omega t + \phi)]^{2n}}. \tag{4.10}$$

Although these parameters are important to our understanding of our model, we only focus on changing the spot lifetime τ, and the seeding rate of these spots with respect to an average pulsation period of a star, s. This way, we are able to focus on the generation rate of the spots and how long they reside on the photosphere.

The parameters shown in Table 4.2 were found to visually fit the actual PA data for Mira and R Leo. The fractional value for τ refers to the fraction of a single spot's total lifetime with respect to a single pulsational period. s is the fractional value of the number of spots randomly generated over the course of one light curve. The value of 0.05 would yield *on average* 50/1000 time increments where a spot contributes its maximum brightness contribution.

TABLE 4.2: Spot lifetime and spot criterion values for o Ceti and R Leo.

Object	τ	s
o Ceti	0.40	0.05
R Leo	0.45	0.05

The data produced by the model includes a time increment, the estimated values of the PA, and the percent polarization for a star with the given constraints. Because most (if not all) observations made by HPOL, Serkowski & Shawl, and Poliakova were made when the stars were near their brightest phase, the same criteria must be applied to the model. So that this criteria is applied, the time intervals in the real data where no observations were made were identified in parallel with the model data, and those intervals within the model data were removed. Otherwise, there would be additional model data that includes times when the star was dim and not observed.

The model was run 300 times for both the B band and the V band per star. Because the spots are generated in a random time and location on the star, each iteration yields a slightly different result. Several runs were performed and their results were averaged in order to assess the best representation of the model with our given parameters. The model's average values for polarization position angle (PA') and amount of polarization (p') were used in calculating σ'_{PA} and σ'_p:

$$\sigma'_{PA}{}^2 = \overline{(PA'^2)} - (\overline{PA'})^2 \tag{4.11}$$

$$\sigma'_p{}^2 = \overline{(p'^2)} - (\overline{p'})^2 \tag{4.12}$$

$\overline{PA'}$ and $\overline{p'}$ are the average values for the polarization angle and the percent of polarization , respectively. The actual data was analyzed in the same fashion to calculate actual values for σ_{PA} and σ_p. Both σ'_{PA} and σ'_p were binned into histograms and compared to σ_{PA} and σ_p for both the B band and the V band in each star.

4.2 Model Results

First, we will show the results of a single iteration of the model. Figure 4.1, Figure 4.2, and Figure 4.3 were created by the model under the parameter constraints $s = 0.05$ and $\tau = 0.45$. In all three of the figures, the values on the vertical axis are all relative magnitudes. The model's light curve, Figure 4.1, is consistent with the light curves of R Leo and Mira in the sense that the light curve peaks are not perfectly uniform. There is some variance in the brightness values at maximum brightness. Figure 4.2 is shown to illustrate the difference between the model's light curve with spots and without spots. There is a clear difference in light curve behavior when spots are added to the model.

The model's time-evolution of PA (Figure 4.3) shows a behavior that is very similar to R Leo and V CVn. A large variance in the values for PA is consistent with our observations. Note that the mean of the model values for PA approach 90° as the number of cycles

increases. Because of this behavior, we were not able to compare the values of PA with the actual values of PA *directly*. Instead, we compared their variances, ${\sigma'_{PA}}^2$ and ${\sigma_{PA}}^2$.

Both Figure 4.4 and Figure 4.5 show the results of the model for both the V band and the B band for the parameter values listed in Table 4.2. The colored dotted lines represent the values for σ_{PA} from the real data. Visually, we see that the model matches the real data better for the V Band than it does for the B band for these two figures.

No dotted lines are shown in Figure 4.6 or in Figure 4.7. Unfortunately, the model's results for σ'_p were not near the actual value for σ_p. As a result, the value for the actual σ_p is off the scale of the figure, but is presented in Table 4.3.

In order to accurately compare the model's mean value of σ with the data's mean value of σ, we used a one sample t-test. Because the model results for polarization (%) were vastly different than the actual values for polarization, it was not necessary to include them in the t-test. The results of the t-test are shown in Table 4.3, which also gives the P values of the t-test.

TABLE 4.3: One sample t-test results for the model and actual σ values

Target	**Model Mean**	**Actual Mean**	**P Value**	**Result**
o Ceti B Band PA	46.67	56.41	<0.0001	Significantly Different
o Ceti V Band PA	47.59	47.99	0.3664	Not Statistically Different
R Leo B Band PA	46.01	54.51	<0.0001	Significantly Different
R Leo V Band PA	46.89	50.33	<0.0001	Significantly Different

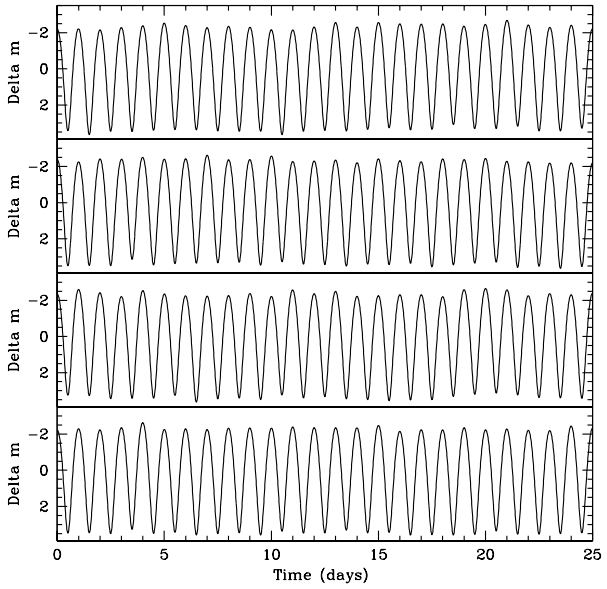

FIGURE 4.1: light curve from a single run of the model with $s = 0.05$ and $\tau = 0.45$, shown in arbitrary magnitudes.

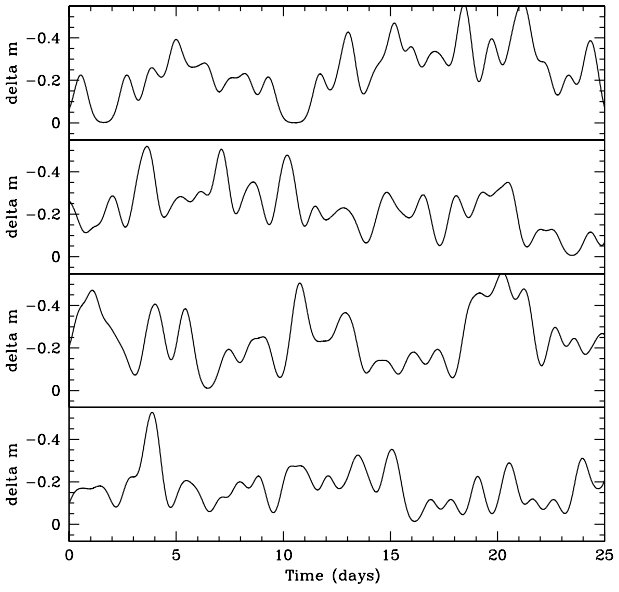

FIGURE 4.2: Differences between the model light curve with spots and the model light curve without the spots, shown in arbitrary magnitudes. This is for a single run of the model with parameters of $s = 0.05$ and $\tau = 0.45$.

4.3 Model Conclusions

Clearly, the model with the parameters listed in Table 4.2 is not an accurate description of the actual polarization values for Mira and R Leo. However, further runs of the

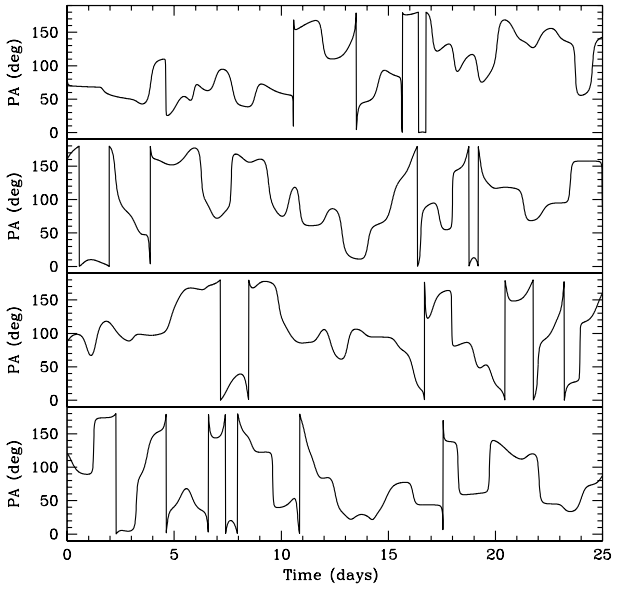

FIGURE 4.3: Polarization angle time evolution for a single run of the model with parameters of $s = 0.05$ and $\tau = 0.45$

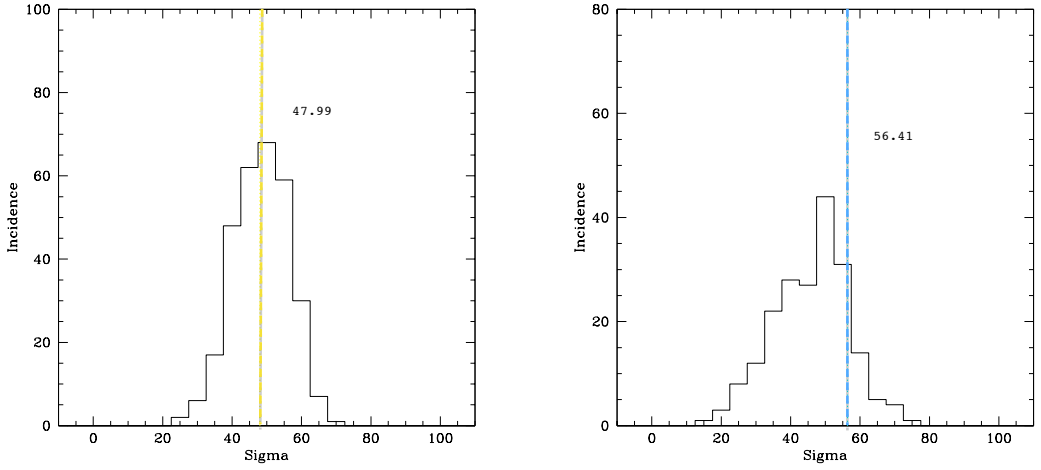

(a) *o* Ceti V band

(b) *o* Ceti B band

FIGURE 4.4: Model results for *o* Ceti PA values in the V band (a) and the B band (b). Values for σ_{PA} are shown as vertical dotted lines.

model could be conducted with the intent to better fit the data. There are many other parameters besides s and τ which could be changed. For example, the light curve duration (N) and the spot temperature enhancement (d) could be manipulated as well.

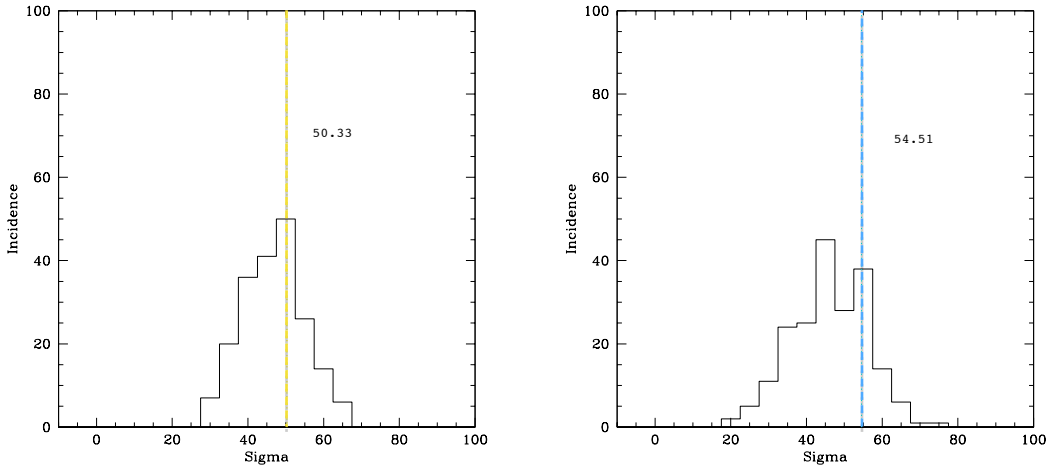

(a) R Leo V band

(b) R Leo B band

FIGURE 4.5: Model results for R Leo PA values in the V band (a) and the B band (b). Values for σ_{PA} are shown as vertical dotted lines.

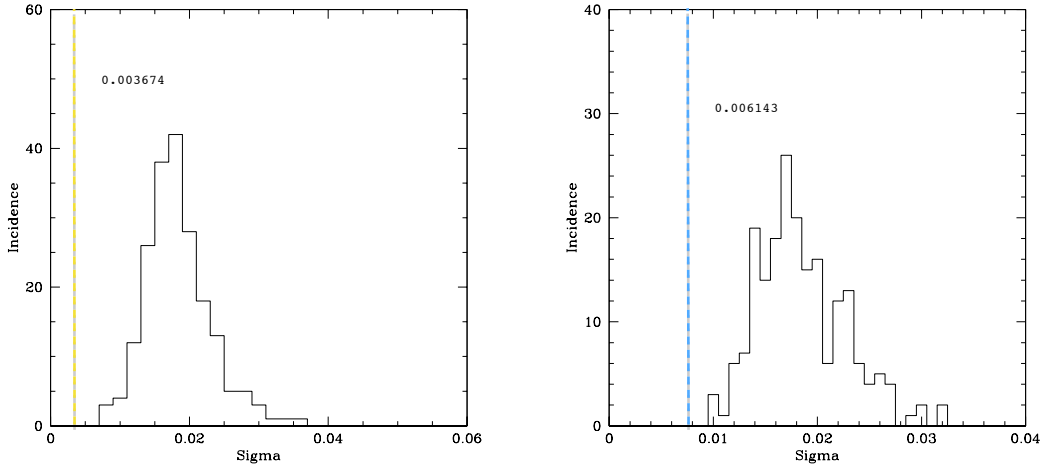

(a) *o* Ceti V band

(b) *o* Ceti B band

FIGURE 4.6: Model results for *o* Ceti Pol(%) values in the V band (a) and the B band (b).

Despite the results of the t-test, the currently used parameters *did* produce large variations in PA, which was the main goal of the model. Further analysis of a model of this type would be an excellent area of future research for Mira stars with polarization properties similar to R Leo and Mira.

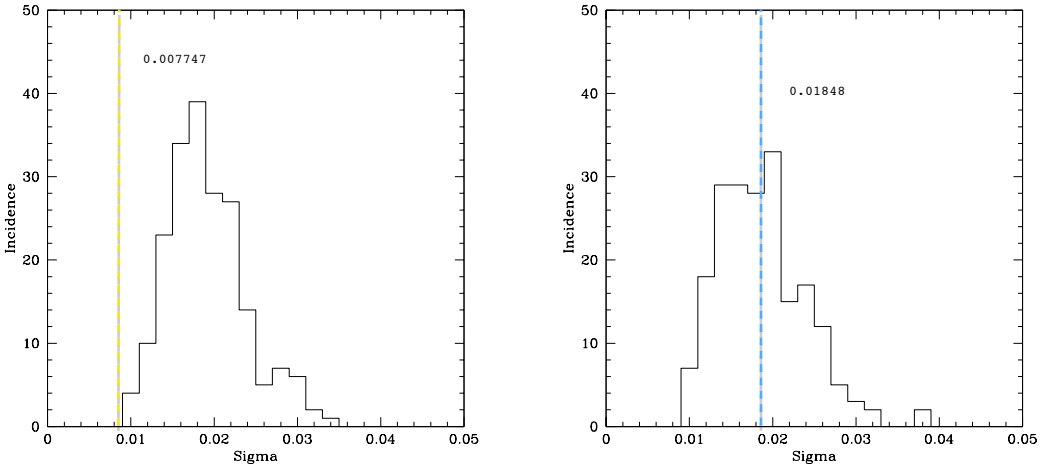

(a) R Leo V band

(b) R Leo B band

FIGURE 4.7: Model results for R Leo Pol(%) values in the V band (a) and the B band (b).

Chapter 5

Conclusions

Mira-type variable stars are fascinating candidates for astrophysical studies because they are known to have several unique properties with respect to other stars on the asymptotic giant branch (AGB) stage of stellar evolution. Their signature characteristic is the brightness variability that can be found in each Mira-type star.

The brightness variability found in these stars is caused by pulsations in a 'shocked' atmosphere (Merrill 1940), which is attributed by the ionization-recombination mechanism within a partially-ionized stellar layer. This mechanism causes optical brightness variations of at least 2.5 magnitudes over periods that last over 100 days (Willson 1976). We sought to develop our understanding about the atmospheric properties of these incredible stars by means of spectropolarimetry.

The motivation for using spectropolarimetric data is to use polarimetry as a probe for identifying geometrical asymmetries in these stars. If a star is unresolved, then it will be revealed with the observation of a polarized continuum (St-Louis et al. 2011). A perfectly spherical distribution of scattering particles within the circumstellar medium would cancel the linear Stokes vectors and no net polarization would be observed (Vink 2011). A non-spherical distribution of scattering particles in an unresolved star would result in some net linear polarization.

We focused our efforts on three stars that have been observed extensively by means of spectropolarimetry: Mira (also referred to as *o* Ceti), R Leo, and V CVn. We collected and used spectropolarimetric data from multiple data archives. Our main source of data was provided by the University of Wisconsin's Half-Wave Spectropolarimeter (HPOL), which can be found at the HPOL website. At the HPOL website, a full table of spectropolarimetric data is given, with additional comments about individual observations.

After performing a cull of the data, only HPOL polarization data with detections of 3σ or higher were tabulated and used in the figures. The values for PA in Mira and R Leo were modified in order to remove artificial PA rotations, which was mainly effective for the PA values of Mira. A tabular journal of the HPOL data used throughout this project is provided in Appendix A.

Besides HPOL, there were two other rich data sets that feature spectropolarimetric data for *o* Ceti, R Leo, and V CVn. Serkowski and Shawl (2001) compiled a very large collection of spectropolarimetric data for 167 different cool variable stars, including RV Tauri stars and classical and Population II Cepheids. Poliakova published the results of polarization observations, including the brightness and color index for V CVn during the years 1980−1986.

We did not subtract the contributions from the ISM in any of our three data sets, since our interest is in the variable polarization characteristics of the stellar source. Although the interstellar medium imposes a polarization signal on starlight, even if that starlight is completely unpolarized upon emission, the interstellar contribution is not expected to vary (e.g., Clarke 2010). Additionally, the means to remove the ISM from each object were not provided from our sources of data.

5.1 Conclusions Regarding Spectropolarimetry Data

Upon viewing the time-evolution of the HPOL data in Chapter 2, we witness remarkable and rapid PA rotations in the UBVRI lightbands for *o* Ceti and R Leo, but not as much for V CVn. In *o* Ceti, nonspherical pulsations, grain growth in the extended atmosphere, and changes in convective cells in the lower atmosphere may play a role in the PA changes (Hayes & Russo 1981). We assume that the unstable and unpredictable nature of the PA is a consequence of a similar, complex atmosphere in R Leo.

Unlike *o* Ceti and R Leo, the PA in each lightband for V CVn is fairly constant before MJD 51000. This indicates the presence of a stable geometry with respect to time. However, the sudden PA rotations in V CVn are fascinating to witness, especially since they occur when the AAVSO light curve changes its pulsation period behavior. It was also useful to examine the incidence of the PA and polarization values in each star. As a consequence, it is easy to see the difference between V CVn and the other two stars.

In Chapter 3, we have seen evidence of the Rayleigh scattering found in previous studies (Harrington 1969; Yudin & Evans 2002). Since electron scattering would produce different time-averages polarization than the ones we obtain, it is safe to assume that

Rayleigh scattering is more favored in these these atmospheres. This observation is consistent with our basic knowledge about these stars. Since Mira-type stars are relatively cool stars (with an effective surface temperature of about 2200 K to 3000 K), we do not expect to see a large amount of free electrons.

On average, Mira variable stars display larger values for polarization than what is expected from a classical model of late-type stars, which is most likely caused by temperature variations on the stellar surface (Harrington 1969). For Mira and V CVn, the polarization increases when hydrogen emission lines become visible (Shawl) which indicates a large number small particles being produced with each pulsation period. This evidence is further supported by Yudin & Evans, who suggest that when polarimetric variability is more evident in the blue, this is evidence of episodic mass ejections that coincide with the formation of small dust particles within the circumstellar environment.

5.2 Conclusions Regarding the Model

In an attempt to understand how R Leo and Mira have such a wide range of values for polarization and PA, we invented a 'toy' model in the spirit of linking basic astrophysical knowledge to our observations. We hypothesize that Mira and R Leo have visibly bright regions in their photospheres, and these spots are responsible for our observed highly variable PA and polarization values. Although Mira stars are not at the same stage of stellar evolution as the Sun, Tomaszewski, Landstreet, McLean et al. (1980) suggest that the polarization of light in Miras is a result of scattering in an atmosphere that is not uniformly bright. Therefore it is safe to hypothesize that Mira stars may have bright regions within their atmosphere.

In the model, we assume a star that is axisymmetric such that the stellar illumination is axisymmetric, and no net polarization would result from non-spherical geometries. It follows that any luminous spot on the stellar surface would result in non-isotropic illumination. Although our model allows a number of variables to affect the outcome of polarization, we only focus on changing the spot lifetime and the seeding rate of these spots with respect to an average pulsation period of a star. This way, we are able to focus on the generation rate of the spots and how long they reside on the photosphere.

After conducting a one sample t-test to the model mean and the data mean, we conclude that the model with our chosen parameters is not an accurate description of the actual polarization values for Mira and R Leo. However, further runs of the model could be conducted with the intent to better fit the data. However, despite the results of the t-test, the currently used parameters *did* produce large variations in PA, which was the

main goal of the model. Further analysis of a model of this type would be an excellent area of future research for Mira stars with polarization properties similar to R Leo and Mira.

5.3 Additional Comments on V CVn

V CVn (officially an SRa variable star) does not display polarimetric properties that are like Mira and R Leo. Instead, it has fairly constant values for PA in each of the five lightband until MJD 51000. After this date, the PA values begin to vary rapidly. This occurs around the same time the AAVSO light curve decreases in brightness variability and the pulsational periods become ambiguous.

Measurements made by Magalhaes, Coyne & Benedetti (1986) on V CVn indicate that absorptions in the TiO band reinforce the idea that most polarization occurs within the photosphere, along with an intermediate scattering layer in the stellar atmosphere. They confirm the model of a pulsating molecular scattering atmosphere which links polarization to the pulsation cycle. Changes within the TiO band are caused by changes in the absorption-to-scattering ratio with respect to optical depth. This is further evidence of a photospheric origin for most optical polarization, along with the presence of an intermediate scattering layer within the stellar atmosphere.

Neilson, Adams, Ignace et al. (2013) suggest that the 40 years of polarimetric observations of V CVn indicate some long-term stable asymmetry that causes consistent values for PA. The observed polarization could be due to the presence of a debris disk that is large enough to produce a constant value for the polarization position angle. This hypothesis is consistent with previous observations of white dwarfs with debris disks (Barber et al. 2012). The presence of such a disk may be an early stage in the development of a binary system of a white dwarf and a companion (Farihi et al. 2005). V CVn would be the first observed semi-regular variable star with a debris disk.

Appendix A

HPOL Synthetic Filter Data

A.1 Mira

UX Band[1]					
MJD	Q(%)	U(%)	σ (%)	P(%)	PA(°)
47800.25	0.3245	−0.7177	0.0357	0.7876	147.16
47825.19	0.2844	−1.0309	0.0363	1.0694	142.71
47853.13	0.2347	0.2440	0.0347	0.3386	23.05
48138.31	−1.1462	0.0734	0.0942	1.1486	88.16
48148.18	−1.6980	−0.2423	0.1368	1.7152	94.06
48154.31	−1.2132	0.3955	0.2955	1.2760	80.97
48161.19	−0.9468	0.3677	0.0287	1.0157	79.38
48166.30	−1.2566	0.4056	0.0830	1.3205	81.05
48175.19	−1.0213	0.4125	0.0271	1.1014	79.00
48191.10	−0.5084	0.3865	0.0246	0.6386	71.38
48196.27	−0.2439	0.4776	0.0378	0.5362	58.52
48203.18	−0.4818	0.2107	0.0312	0.5259	78.19
48208.09	−0.3890	0.1280	0.0844	0.4095	80.89
48219.05	−0.1088	−0.0398	0.0248	0.1159	100.05
48284.02	0.3749	−1.0213	0.1636	1.0880	145.08
48313.01	−1.6926	−2.3400	0.5962	2.8880	117.06
48493.35	0.4476	−1.1714	0.3448	1.2540	145.46
48500.26	0.3260	−0.7088	0.0949	0.7802	147.35
48538.18	0.2297	−0.0951	0.0424	0.2486	168.76
49231.36	−0.1218	0.2519	0.0453	0.2798	57.90
51475.66	−0.7491	−0.0340	0.1405	0.7498	91.30
51485.71	−0.2842	0.6028	0.0877	0.6665	57.62
51564.55	−0.2932	−0.7905	0.2440	0.8431	124.83
51835.71	−1.6352	1.5386	0.6074	2.2452	68.37
51851.66	−0.0014	2.1309	0.1515	2.1309	45.02
52275.70	0.7217	0.0834	0.1053	0.7265	3.30
52520.88	−1.3615	1.3981	0.1778	1.9515	67.12
52582.74	1.3583	5.1022	0.7307	5.2799	37.54
52619.58	1.3443	1.7730	0.6922	2.2250	26.42
53258.86	1.7703	1.1943	0.6921	2.1355	17.00

[1] 54.5% of the original data is not included.

V Band[2]

MJD	Q(%)	U(%)	σ (%)	P(%)	PA(°)
47800.25	0.0793	−0.2806	0.0010	0.2916	142.89
47825.19	0.0198	−0.1342	0.0009	0.1357	139.20
47842.18	0.0786	−0.0286	0.0015	0.0836	169.99
47853.13	0.0863	0.0175	0.0011	0.0881	5.74
47860.10	0.1129	0.0456	0.0046	0.1218	11.00
47867.06	0.0945	0.0323	0.0013	0.0999	9.45
47873.09	0.0968	0.0433	0.0014	0.1060	12.05
48138.31	−0.2511	0.2099	0.0022	0.3273	70.06
48148.18	−0.2541	0.3656	0.0038	0.4453	62.40
48154.31	−0.2668	0.3740	0.0029	0.4594	62.75
48161.19	−0.3182	0.4478	0.0010	0.5493	62.70
48166.30	−0.3479	0.4946	0.0019	0.6047	62.56
48175.19	−0.3847	0.5612	0.0009	0.6804	62.21
48191.10	−0.2635	0.4972	0.0011	0.5627	58.96
48196.27	−0.1949	0.4320	0.0015	0.4739	57.14
48203.18	−0.1371	0.3611	0.0013	0.3863	55.40
48208.09	−0.1213	0.3136	0.0014	0.3362	55.57
48219.05	−0.0869	0.2416	0.0011	0.2567	54.90
48259.05	−0.0057	0.1455	0.0034	0.1456	46.13
48284.02	0.0513	0.0491	0.0060	0.0710	21.87
48297.08	0.0979	−0.0077	0.0257	0.0982	177.75
48313.01	0.2403	−0.0890	0.0256	0.2563	169.84
48493.35	0.4353	−0.1991	0.0023	0.4786	167.71
48500.26	0.4477	−0.1693	0.0029	0.4786	169.64
48538.18	0.1742	−0.0137	0.0019	0.1747	177.75
48569.22	0.1078	−0.0567	0.0036	0.1218	166.12
48599.14	0.0987	−0.0892	0.0053	0.1330	158.95
48633.05	0.0055	−0.0631	0.0089	0.0633	137.51
49231.36	0.1473	0.0719	0.0043	0.1639	13.01
49589.30	0.1047	0.0976	0.0159	0.1432	21.49
49638.30	0.0904	0.3065	0.0270	0.3196	36.78
49666.14	−0.0779	0.3007	0.0152	0.3106	52.26
49713.09	0.0676	0.3393	0.0314	0.3459	39.36
49715.01	0.0425	0.5503	0.0353	0.5519	42.79
50715.91	−0.2826	0.5448	0.0223	0.6049	58.92
50731.75	−0.3339	0.7105	0.0241	0.7850	57.58
51161.63	0.0846	0.3560	0.0023	0.3659	38.31
51422.79	−0.0111	0.1504	0.0140	0.1508	47.10
51424.82	0.1159	−0.0031	0.0173	0.1159	179.24
51458.72	0.0933	0.0564	0.0036	0.1090	15.58
51466.75	0.0965	0.0316	0.0024	0.1015	9.07
51475.66	0.1210	0.0430	0.0015	0.1284	9.78
51485.71	0.1032	0.0630	0.0014	0.1209	15.70
51503.62	0.1402	0.0500	0.0026	0.1489	9.81
51521.59	0.1523	−0.0387	0.0202	0.1571	172.88
51529.60	0.1018	0.0068	0.0019	0.1020	1.91
51557.63	0.0923	0.0350	0.0061	0.0987	10.38
51562.50	0.0693	0.0201	0.0033	0.0721	8.09
51564.55	0.0622	0.0065	0.0033	0.0625	2.98
51835.71	−0.0933	0.5141	0.0024	0.5225	50.14
51851.66	−0.0705	0.4945	0.0023	0.4995	49.06
51961.52	0.4052	0.6296	0.0863	0.7487	28.62

[2] 10.6% of the original data is not included.

V Band Continued

MJD	Q(%)	U(%)	σ (%)	P(%)	PA(°)
52224.73	0.0384	0.0335	0.0039	0.0510	20.56
52275.70	0.0503	0.0019	0.0040	0.0503	1.08
52520.88	−0.3215	0.2653	0.0038	0.4168	70.23
52582.74	−0.2483	0.4117	0.0055	0.4807	60.55
52618.68	−0.0714	0.7635	0.0393	0.7669	47.67
52619.58	−0.3800	0.6842	0.0511	0.7826	59.52
53258.86	−0.0857	0.7671	0.0251	0.7719	48.19

B Band[3]

MJD	Q(%)	U(%)	σ (%)	P(%)	PA(°)
47800.25	0.1844	−0.4963	0.0018	0.5295	145.19
47825.19	0.0957	−0.1555	0.0018	0.1826	150.81
47842.18	0.1357	0.0480	0.0027	0.1440	9.73
47853.13	0.1424	0.1005	0.0021	0.1743	17.61
47860.10	0.1530	0.1324	0.0093	0.2023	20.43
47867.06	0.1487	0.1385	0.0027	0.2032	21.48
47873.09	0.1318	0.1690	0.0027	0.2144	26.02
48138.31	−0.9342	0.3009	0.0062	0.9815	81.08
48148.18	−0.8246	0.5542	0.0089	0.9935	73.05
48154.31	−0.7998	0.5970	0.0067	0.9981	71.63
48161.19	−0.8261	0.5841	0.0022	1.0118	72.37
48166.30	−0.8723	0.6485	0.0043	1.0870	71.69
48175.19	−0.8489	0.7250	0.0019	1.1164	69.75
48191.10	−0.5517	0.6016	0.0023	0.8162	66.26
48196.27	−0.4159	0.5440	0.0036	0.6847	63.70
48203.18	−0.3119	0.4020	0.0027	0.5088	63.90
48208.09	−0.2411	0.2977	0.0032	0.3831	64.50
48219.05	−0.1726	0.1575	0.0021	0.2337	68.81
48259.05	0.0723	−0.1527	0.0084	0.1690	147.67
48281.04	0.3455	−0.3067	0.0876	0.4620	159.20
48284.02	0.2371	−0.4065	0.0155	0.4706	150.12
48297.08	0.2008	−0.3140	0.0962	0.3728	151.30
48313.01	0.0456	−0.9906	0.1016	0.9916	136.32
48493.35	0.4091	−0.4744	0.0053	0.6264	155.39
48500.26	0.4023	−0.3800	0.0057	0.5534	158.31
48538.18	0.1432	−0.0412	0.0041	0.1490	171.97
48569.22	0.1182	−0.0479	0.0085	0.1275	168.98
48599.14	0.1499	−0.1844	0.0143	0.2376	154.56
48633.05	0.1764	−0.1767	0.0221	0.2497	157.48
48661.01	0.2164	−0.0951	0.0401	0.2364	168.14
49231.36	0.2926	−0.0351	0.0076	0.2947	176.58
49589.30	−0.0063	−0.2228	0.0396	0.2229	134.19
49638.30	0.1563	0.5990	0.0472	0.6191	37.69
49666.14	0.5112	0.5360	0.0298	0.7407	23.18
49713.09	0.5409	0.6819	0.0531	0.8703	25.79
49715.01	0.7715	0.8544	0.0743	1.1512	23.96
50715.91	−0.1820	0.5259	0.1531	0.5565	54.55
50731.75	0.2457	2.7911	0.1713	2.8019	42.49
51161.63	0.1810	1.0080	0.0071	1.0241	39.91
51422.79	0.0821	0.2130	0.0721	0.2283	34.46
51424.82	0.4808	0.1752	0.1632	0.5117	10.01
51458.72	0.2255	0.0061	0.0109	0.2256	0.77
51466.75	0.2269	−0.0217	0.0071	0.2279	177.27
51475.66	0.2133	0.0363	0.0034	0.2163	4.82
51485.71	0.1623	0.1301	0.0031	0.2080	19.35
51503.62	0.2221	0.1083	0.0073	0.2472	13.00
51529.60	0.0929	0.0410	0.0051	0.1015	11.92
51557.63	−0.1737	0.0779	0.0331	0.1904	77.92
51562.50	0.0845	0.0916	0.0085	0.1246	23.65
51564.55	0.0644	0.0216	0.0124	0.0679	9.28
51835.71	−0.1964	1.0870	0.0074	1.1046	50.12
51851.66	−0.1676	1.0936	0.0059	1.1064	49.36

[3] 9.1% of the original data is not included.

B Band Continued

MJD	Q(%)	U(%)	σ (%)	P(%)	PA(°)
51961.52	1.0997	1.0279	0.2513	1.5053	21.53
52224.73	−0.0882	0.3577	0.0178	0.3684	51.92
52275.70	0.0947	0.1744	0.0122	0.1984	30.74
52520.88	−0.8153	0.8239	0.0140	1.1591	67.35
52582.74	−0.6931	1.5129	0.0427	1.6641	57.31
52618.68	1.2632	0.3596	0.2872	1.3134	7.95
52619.58	−0.4595	1.2291	0.1726	1.3122	55.25
53258.86	−0.1256	1.3783	0.0766	1.3841	47.60

R Band[4]

MJD	Q(%)	U(%)	σ (%)	P(%)	PA(°)
47800.25	0.0380	−0.1254	0.0008	0.1310	143.44
47825.19	0.0025	−0.0694	0.0007	0.0695	136.02
47842.18	0.0436	−0.0032	0.0016	0.0437	177.88
47853.13	0.0522	0.0274	0.0011	0.0590	13.85
47860.10	0.0601	0.0698	0.0047	0.0921	24.65
47867.06	0.0584	0.0350	0.0012	0.0681	15.48
47873.09	0.0492	0.0401	0.0014	0.0635	19.60
48138.31	−0.0608	0.1379	0.0020	0.1507	56.90
48148.18	−0.0731	0.2028	0.0032	0.2156	54.91
48154.31	−0.0650	0.1663	0.0032	0.1785	55.68
48161.19	−0.1027	0.2453	0.0010	0.2659	56.36
48166.30	−0.1195	0.2624	0.0021	0.2883	57.24
48175.19	−0.1388	0.3034	0.0009	0.3337	57.30
48191.10	−0.0879	0.2588	0.0011	0.2733	54.38
48196.27	−0.0634	0.2371	0.0014	0.2455	52.48
48203.18	−0.0323	0.1836	0.0013	0.1864	49.98
48208.09	−0.0446	0.1527	0.0014	0.1591	53.15
48219.05	−0.0178	0.1261	0.0010	0.1273	49.02
48259.05	0.0168	0.0593	0.0026	0.0616	37.11
48281.04	0.0323	0.0929	0.0182	0.0984	35.41
48284.02	0.0680	0.0046	0.0043	0.0681	1.93
48297.08	0.1101	0.0055	0.0131	0.1102	1.44
48313.01	0.0821	−0.0470	0.0151	0.0946	165.10
48493.35	0.2041	−0.0304	0.0021	0.2064	175.77
48500.26	0.2044	−0.0332	0.0028	0.2071	175.39
48538.18	0.0822	0.0334	0.0017	0.0887	11.07
48569.22	0.0856	0.0371	0.0025	0.0933	11.72
48599.14	0.0514	−0.0074	0.0034	0.0519	175.91
48633.05	0.0711	0.0117	0.0055	0.0721	4.67
48661.01	0.0545	0.0085	0.0078	0.0551	4.45
49231.36	0.1174	0.0187	0.0033	0.1189	4.52
49589.30	0.0323	0.1123	0.0118	0.1169	36.97
49638.30	−0.0088	0.1517	0.0169	0.1520	46.66
49666.14	−0.0179	0.1701	0.0093	0.1711	48.01
49713.09	0.0457	0.1075	0.0182	0.1168	33.48
49715.01	0.0595	0.0986	0.0199	0.1151	29.45
50703.86	−0.0083	0.2956	0.0026	0.2957	45.81
51161.63	0.0217	0.1842	0.0017	0.1855	41.64
51422.79	0.0591	0.1025	0.0027	0.1183	30.02
51458.72	0.0526	0.0504	0.0014	0.0728	21.89
51466.75	0.0486	0.0347	0.0011	0.0597	17.79
51475.66	0.0569	0.0351	0.0012	0.0669	15.84
51485.71	0.0538	0.0648	0.0012	0.0842	25.17
51503.62	0.0739	0.0485	0.0034	0.0884	16.65
51521.59	0.0635	−0.0054	0.0084	0.0637	177.58
51557.63	0.0402	0.0882	0.0022	0.0969	32.75
51562.50	0.0216	0.0807	0.0020	0.0836	37.51
51606.53	−0.0295	0.0772	0.0074	0.0826	55.45
51607.54	−0.0400	0.0766	0.0071	0.0864	58.80
51830.67	−0.1460	0.2950	0.0117	0.3291	58.17
51835.71	−0.0282	0.2875	0.0020	0.2889	47.80
51851.66	−0.0258	0.2694	0.0020	0.2707	47.73

[4] 9.1% of the original data is not included.

R Band Continued

MJD	Q(%)	U(%)	σ (%)	P(%)	PA(°)
51961.52	0.1788	0.2033	0.0159	0.2707	24.34
52224.73	−0.0108	0.0492	0.0013	0.0504	51.19
52275.70	−0.0209	0.0363	0.0023	0.0418	59.99
52520.88	−0.2244	0.1795	0.0020	0.2874	70.67
52582.74	−0.1630	0.2396	0.0011	0.2897	62.11
52618.68	−0.1444	0.3143	0.0137	0.3459	57.34
52619.58	−0.2118	0.3465	0.0160	0.4061	60.72
53258.86	−0.0180	0.3970	0.0090	0.3974	46.30

I Band[5]

MJD	Q(%)	U(%)	σ (%)	P(%)	PA(°)
47800.25	0.0199	−0.0991	0.0015	0.1011	140.67
47825.19	−0.0099	−0.0365	0.0015	0.0378	127.38
47842.18	0.0232	0.0170	0.0040	0.0288	18.12
47853.13	0.0392	0.0332	0.0026	0.0514	20.15
47860.10	0.0119	0.0789	0.0107	0.0797	40.72
47867.06	0.0513	0.0475	0.0027	0.0700	21.39
47873.09	0.0345	0.0536	0.0029	0.0638	28.61
48138.31	−0.1117	0.0828	0.0045	0.1391	71.72
48148.18	−0.0972	0.1217	0.0082	0.1557	64.30
48154.31	−0.0614	0.0299	0.0091	0.0683	77.00
48161.19	−0.1093	0.1166	0.0027	0.1598	66.57
48166.30	−0.101	0.1204	0.0055	0.1572	65.00
48175.19	−0.0962	0.1547	0.0024	0.1822	60.93
48191.10	−0.0427	0.1020	0.0028	0.1106	56.36
48196.27	−0.0463	0.1191	0.0040	0.1278	55.61
48203.18	0.0060	0.0799	0.0031	0.0801	42.87
48208.09	−0.0401	0.0463	0.0036	0.0613	65.47
48219.05	−0.0045	0.0592	0.0022	0.0594	47.18
48284.02	0.0540	−0.0359	0.0077	0.0648	163.19
48297.08	0.1356	−0.0296	0.0236	0.1388	173.85
48313.01	0.0934	−0.1276	0.0251	0.1582	153.10
48493.35	0.1010	0.0421	0.0044	0.1094	11.31
48500.26	0.1151	0.0215	0.0057	0.1171	5.30
48538.18	0.0489	0.0804	0.0034	0.0941	29.36
48569.22	0.0841	0.0864	0.0043	0.1206	22.90
48599.14	0.0492	0.0129	0.0059	0.0508	7.35
48633.05	0.1009	0.0340	0.0095	0.1065	9.32
48661.01	0.0916	0.0141	0.0136	0.0926	4.37
49231.36	0.0969	−0.0264	0.0067	0.1004	172.38
49589.30	−0.0489	0.1716	0.0242	0.1784	52.95
49638.30	−0.0430	0.2296	0.0304	0.2336	50.31
49666.14	−0.0199	0.1697	0.0168	0.1708	48.34
49715.01	0.0673	0.1180	0.0367	0.1359	30.16
50703.86	−0.0424	0.3447	0.0014	0.3473	48.51
51161.63	0.0181	0.1831	0.0010	0.1840	42.18
51422.79	0.0616	0.0816	0.0014	0.1022	26.48
51458.72	0.0332	0.0482	0.0009	0.0585	27.70
51466.75	0.0310	0.0427	0.0007	0.0528	27.01
51475.66	0.0394	0.0500	0.0008	0.0636	25.88
51485.71	0.0416	0.0806	0.0008	0.0907	31.36
51503.62	0.0413	0.0617	0.0022	0.0743	28.10
51521.59	0.0193	0.0882	0.0039	0.0902	38.83
51557.63	0.0054	0.1083	0.0012	0.1084	43.57
51562.50	0.0023	0.0845	0.0012	0.0845	44.24
51606.53	−0.0641	0.1466	0.0025	0.1601	56.81
51607.54	−0.0704	0.1590	0.0020	0.1739	56.94
51830.67	−0.0541	0.2844	0.0036	0.2895	50.39
51835.71	−0.0336	0.2781	0.0013	0.2801	48.45
51851.66	−0.0063	0.2594	0.0013	0.2594	45.70
51961.52	0.0894	0.1381	0.0031	0.1645	28.54
52224.73	−0.0591	0.0586	0.0008	0.0832	67.62
52275.70	−0.0684	0.1083	0.0013	0.1281	61.14

[5] 12.1% of the original data is not included.

I Band Continued

MJD	Q(%)	U(%)	σ (%)	P(%)	PA(°)
52520.88	−0.2053	0.1798	0.0013	0.2729	69.39
52582.74	−0.1956	0.2155	0.0007	0.2910	66.11
52618.68	−0.1735	0.2148	0.0041	0.2761	64.46
52619.58	−0.1681	0.2091	0.0039	0.2683	64.39
52994.59	−0.0901	0.2203	0.0066	0.2380	56.12
53258.86	0.0430	0.3184	0.0026	0.3213	41.15

A.2 R Leo

UX Band[6]

MJD	Q(%)	U(%)	σ (%)	P(%)	PA(°)
47952.23	−0.8349	−2.2285	0.4438	2.3798	124.73
48000.07	−0.5527	−1.7816	0.5669	1.8654	126.38
50080.79	1.8747	0.1712	0.3499	1.8825	2.61
50796.80	−0.1668	2.5785	0.1857	2.5839	46.85
50797.85	1.6217	2.9464	0.2012	3.3632	30.59
50823.76	1.1634	4.0440	0.5269	4.2080	36.98
51170.82	4.0332	1.9191	0.7531	4.4665	12.72
51607.73	2.1033	−4.1341	0.8815	4.6384	148.48
51661.60	−0.8057	−1.9794	0.3771	2.1371	123.93
51964.71	−0.7605	0.8704	0.2388	1.1558	65.57
51994.62	2.0582	1.1874	0.4522	2.3762	14.99
52024.58	−2.018	−0.5210	0.6199	2.0842	97.24

V Band[7]

MJD	Q(%)	U(%)	σ (%)	P(%)	PA(°)
47606.09	−0.0101	0.0352	0.0036	0.0366	52.96
47952.23	0.0930	0.2267	0.0050	0.2450	33.85
48000.07	−0.2758	0.0730	0.0089	0.2853	82.59
48330.17	−0.0107	0.5454	0.0092	0.5455	45.56
49761.71	0.6164	2.0712	0.0476	2.1610	36.71
49800.66	−0.0199	1.4830	0.0044	1.4831	45.38
50080.79	0.3485	−0.1338	0.0052	0.3734	169.50
50578.58	−0.5603	0.0876	0.0271	0.5671	85.56
50796.80	0.3183	1.7325	0.0048	1.7615	39.79
50797.85	0.4582	1.8716	0.0072	1.9269	38.12
50823.76	0.5933	1.3757	0.0075	1.4981	33.34
50894.65	0.2805	0.0811	0.0471	0.2920	8.07
50939.63	−0.4020	−0.6157	0.0684	0.7353	118.43
51170.82	0.2068	−0.5414	0.0086	0.5796	145.45
51208.81	0.1463	−0.2164	0.0278	0.2612	152.03
51231.79	−0.0248	−0.5388	0.0468	0.5394	133.68
51522.84	0.4344	−0.2506	0.0805	0.5015	165.01
51562.70	0.6355	−0.7622	0.0257	0.9924	154.91
51606.79	0.3477	−0.8088	0.0129	0.8804	146.63
51607.73	0.4193	−0.8214	0.0115	0.9222	148.52
51658.60	0.6441	−0.9151	0.0042	1.1190	152.57
51661.60	0.7250	−1.0868	0.0053	1.3065	151.85
51677.62	0.3594	−0.9878	0.0051	1.0512	145.00
51964.71	−0.0735	−0.2442	0.0027	0.2550	126.62
51994.62	−0.1018	−0.2069	0.0033	0.2306	121.90
52024.58	−0.0983	−0.1754	0.0083	0.2011	120.37
52028.59	−0.0779	−0.1951	0.0067	0.2101	124.11
52409.61	−0.1313	−0.0731	0.0168	0.1502	104.55
52619.91	0.5477	−0.0424	0.0045	0.5494	177.79
53061.64	0.6739	−0.7442	0.0947	1.0040	156.08

[6] 68.4% of the original data is not included.
[7] 21.1% of the original data is not included.

B Band[8]

MJD	Q(%)	U(%)	σ (%)	P(%)	PA(°)
47606.09	−0.0071	0.2599	0.0063	0.2600	45.78
47952.23	−0.5527	−0.9292	0.0097	1.0812	119.63
48000.07	−0.7856	−0.9751	0.0198	1.2522	115.57
48330.17	0.6349	0.5500	0.0238	0.8401	20.45
49761.71	1.6346	4.4050	0.4591	4.6985	34.82
49800.66	0.3844	3.1487	0.0154	3.1721	41.52
50080.79	0.7654	−0.1166	0.0178	0.7743	175.67
50578.58	−0.6827	1.5418	0.1816	1.6862	56.94
50796.80	0.6254	3.5565	0.0216	3.6110	40.01
50797.85	0.6111	3.7112	0.0298	3.7611	40.32
50823.76	0.6094	2.3142	0.0476	2.3931	37.62
50939.63	−3.5843	−0.7961	0.7290	3.6717	96.26
51170.82	0.0687	−0.1385	0.0618	0.1546	148.19
51208.81	−0.8899	1.4297	0.2865	1.6840	60.95
51231.79	−0.9753	−0.8944	0.3871	1.3233	111.26
51562.70	2.1831	−0.2771	0.3473	2.2007	176.38
51606.79	3.6406	−1.6659	0.1525	4.0036	167.71
51607.73	2.8933	−0.6687	0.0758	2.9695	173.49
51658.60	1.0899	−1.9313	0.0205	2.2176	149.72
51661.60	1.1076	−1.8191	0.0236	2.1297	150.67
51677.62	0.2334	−1.315	0.0405	1.3355	140.03
51964.71	−0.0561	0.2514	0.0115	0.2576	51.29
51994.62	−0.1563	0.3334	0.0129	0.3682	57.56
52024.58	−0.0249	0.4739	0.0471	0.4745	46.50
52028.59	−0.2581	0.4729	0.0398	0.5388	59.31
52409.61	−1.9077	1.1612	0.6580	2.2333	74.34
52619.91	1.1696	−0.0012	0.0215	1.1696	179.97

[8] 26.3% of the original data is not included.

R Band[9]

MJD	Q(%)	U(%)	σ (%)	P(%)	PA(°)
47606.09	0.0290	0.0377	0.0025	0.0476	26.24
47952.23	0.0205	0.1352	0.0041	0.1368	40.69
48000.07	−0.1469	0.1440	0.0059	0.2057	67.79
48330.17	−0.1069	0.3699	0.0061	0.3851	53.06
49761.71	0.4175	0.7615	0.0087	0.8685	30.63
49800.66	0.1739	0.4860	0.0023	0.5162	35.16
50080.79	0.2757	−0.1616	0.0017	0.3196	164.81
50107.85	0.3139	−0.1633	0.0018	0.3538	166.26
50578.58	−0.1007	−0.0043	0.0036	0.1008	91.22
50796.80	0.2159	0.8276	0.0015	0.8553	37.69
50823.76	0.3460	0.5609	0.0025	0.6591	29.17
50894.65	0.0398	−0.1830	0.0043	0.1873	141.14
50927.66	−0.1257	−0.3026	0.0059	0.3277	123.72
50939.63	−0.1454	−0.4349	0.0039	0.4586	125.76
51143.98	0.0867	−0.3930	0.0019	0.4025	141.22
51170.82	0.2007	−0.3816	0.0026	0.4312	148.87
51208.81	0.2602	−0.2844	0.0049	0.3855	156.23
51231.79	0.0118	−0.0270	0.0008	0.0295	146.78
51239.64	0.2898	−0.2884	0.0109	0.4089	157.57
51562.70	0.2554	−0.5541	0.0050	0.6101	147.38
51606.79	0.2168	−0.6070	0.0026	0.6445	144.83
51658.60	0.2597	−0.6366	0.0013	0.6875	146.10
51677.62	0.0007	−0.6681	0.0018	0.6681	135.03
51964.71	0.0206	−0.1892	0.0013	0.1903	138.10
51994.62	0.0055	−0.1566	0.0019	0.1567	136.00
52024.58	0.0044	−0.1524	0.0016	0.1525	135.84
52409.61	−0.1239	0.0257	0.0113	0.1266	84.14
52619.91	0.3232	−0.0436	0.0015	0.3261	176.16
52994.82	−0.3244	0.0418	0.0057	0.3271	86.33
53057.62	0.0219	0.1558	0.0171	0.1573	41.01
53061.64	0.3579	−0.0238	0.0135	0.3587	178.10
53115.60	−0.5388	−0.3760	0.0117	0.6570	107.50

[9] 15.8% of the original data is not included.

I Band[10]

MJD	Q(%)	U(%)	σ (%)	P(%)	PA(°)
47606.09	0.1134	0.1265	0.0045	0.1699	24.07
47952.23	−0.1629	0.0559	0.0082	0.1722	80.54
48000.07	−0.2030	0.0745	0.0124	0.2163	79.92
48330.17	−0.1288	0.3468	0.0114	0.3699	55.19
49761.71	0.4698	0.7178	0.0018	0.8579	28.40
49800.66	0.3254	0.4507	0.0010	0.5559	27.09
50080.79	0.3323	−0.1004	0.0009	0.3471	171.59
50107.85	0.3814	−0.0836	0.0010	0.3905	173.82
50578.58	0.1242	0.1555	0.0016	0.1990	25.70
50796.80	0.2349	0.6741	0.0009	0.7138	35.39
50823.76	0.3056	0.3130	0.0014	0.4375	22.85
50894.65	−0.1222	−0.3914	0.0019	0.4101	126.33
50927.66	−0.1845	−0.5292	0.0020	0.5605	125.39
50939.63	−0.1834	−0.5579	0.0017	0.5873	125.90
51143.98	0.2102	−0.3674	0.0010	0.4233	149.89
51170.82	0.2958	−0.3227	0.0013	0.4377	156.26
51208.81	0.2966	−0.2930	0.0018	0.4169	157.67
51231.79	0.0188	−0.0239	0.0002	0.0304	154.11
51239.64	0.2781	−0.3532	0.0049	0.4495	154.11
51562.70	0.2285	−0.4929	0.0025	0.5433	147.44
51606.79	0.2505	−0.6867	0.0014	0.7310	145.02
51658.60	0.2434	−0.6777	0.0009	0.7200	144.88
51677.62	−0.0142	−0.6781	0.0015	0.6783	134.40
51964.71	0.1336	−0.1362	0.0008	0.1908	157.23
51994.62	0.1247	−0.1113	0.0013	0.1672	159.13
52024.58	0.0797	−0.1293	0.0010	0.1519	150.83
52409.61	−0.1443	−0.0712	0.0086	0.1609	103.14
52619.91	0.3348	0.0347	0.0010	0.3366	2.96
52994.82	−0.2299	0.1014	0.0022	0.2513	78.10
53057.62	0.4524	0.1587	0.0033	0.4794	9.67
53061.64	0.5240	0.1391	0.0034	0.5422	7.43
53115.60	−0.6875	−0.4296	0.0031	0.8107	106.00

[10] 15.8% of the original data is not included.

A.3 V-CVn

		UX Band[11]			
MJD	Q(%)	U(%)	σ (%)	P(%)	PA(°)
47596.22	−0.9156	−1.1012	0.1419	1.4321	115.13
47613.14	−1.1931	−0.2945	0.3113	1.2289	96.93
47897.38	−2.9758	−1.3167	0.2839	3.2541	101.93
47898.38	−3.9341	−1.4350	0.2615	4.1876	100.02
47920.30	−3.0310	−1.9187	0.1099	3.5873	106.17
47928.34	−2.8256	−1.7450	0.1465	3.3210	105.85
47951.17	−2.5118	0.7638	0.3476	2.6254	81.54
47985.14	−2.4488	−1.7234	0.7867	2.9944	107.57
47997.10	−1.7874	−0.5304	0.5712	1.8644	98.26
48085.10	−5.1892	−0.2837	0.7992	5.1970	91.57
48105.10	−5.0312	−0.0208	0.8536	5.0313	90.12
48344.19	−2.7114	−1.6258	0.3829	3.1615	105.47
48386.14	−1.5299	−1.6854	0.3572	2.2762	113.88
48403.15	−1.5366	0.1782	0.3727	1.5469	86.69
48632.39	−6.7659	−2.2834	1.6867	7.1409	99.33
48654.34	−8.0099	0.7584	1.4420	8.0457	87.30
48705.17	−2.9229	−1.5239	0.9024	3.2963	103.77
48760.13	−2.9444	−0.1370	0.3293	2.9476	91.33
48770.10	−2.2036	−0.1130	0.4124	2.2065	91.47
48794.17	−2.3308	−1.3890	0.8206	2.7133	105.40
48976.39	−0.8963	−0.7829	0.1416	1.1900	110.60
49036.23	−4.1256	−2.3542	0.5218	4.7501	104.86
49063.27	−4.8611	−2.5294	0.4035	5.4798	103.75
49098.14	−2.1650	−2.2016	0.1577	3.0878	112.74
49120.14	−1.1916	−1.2981	0.1838	1.7621	113.73
49361.46	−1.1781	−0.6177	0.1551	1.3302	103.84
49410.34	−4.9607	−3.0142	0.1997	5.8047	105.64
49442.19	−6.4903	−1.2869	0.2236	6.6167	95.61
49461.26	−3.9427	−1.4295	0.5557	4.1939	99.97
49510.10	−3.1602	1.1016	0.7408	3.3467	80.39
49793.70	−2.9284	4.2613	1.4546	5.1705	62.25
49812.73	−5.5371	−1.1840	1.3529	5.6622	96.04
49856.65	−2.3133	−0.4203	0.2493	2.3511	95.15
50123.89	−2.3691	−1.0931	0.1840	2.6091	102.38
50519.78	−3.4113	−3.1222	0.7405	4.6244	111.23
50908.69	−3.4181	−1.8644	1.2001	3.8935	104.31
51161.94	−7.3891	−3.2381	1.1937	8.0675	101.83
51195.86	−1.4616	−3.5826	1.2825	3.8693	123.90
51223.84	−1.9495	−3.7384	0.9040	4.2162	121.23
51564.89	1.4777	−3.1850	0.7661	3.5111	147.45
51685.70	6.7256	−1.4194	1.0513	6.8737	174.04
51906.90	−1.1025	−9.7256	2.8888	9.7879	131.77
51929.87	1.7736	−2.5548	0.8983	3.1101	152.38
51972.67	1.1866	5.4082	1.0860	5.5369	38.81
52041.66	−1.8279	4.5016	1.1544	4.8586	56.05
52089.63	3.7078	−3.2025	1.3876	4.8994	159.59
52319.86	7.0639	−4.8474	1.6546	8.5671	162.77
52436.64	2.2851	−15.250	2.4655	15.421	139.26
52856.58	−0.9140	−14.680	1.6227	14.709	133.22

[11] 46.8% of the original data is not included.

V Band[12]

MJD	Q(%)	U(%)	σ (%)	P(%)	PA(°)
47596.22	−0.9659	0.0604	0.0107	0.9678	88.21
47613.14	−0.8089	0.1418	0.0211	0.8213	85.03
47897.38	−1.8663	0.0372	0.0214	1.8666	89.43
47898.38	−1.8431	−0.0022	0.0109	1.8431	90.03
47920.30	−2.6700	−0.2813	0.0062	2.6848	93.01
47928.34	−2.5865	−0.4028	0.0092	2.6176	94.43
47951.17	−1.9614	−0.1818	0.0049	1.9698	92.65
47977.22	−1.3161	0.0214	0.0068	1.3163	89.54
47985.14	−1.2461	0.0831	0.0162	1.2489	88.09
47986.10	−1.1942	0.0357	0.0142	1.1947	89.14
47997.10	−0.9161	−0.0580	0.0045	0.9180	91.81
48047.13	−1.5679	−0.5448	0.0110	1.6598	99.58
48085.10	−3.5070	0.2047	0.0132	3.5130	88.33
48091.11	−3.5363	−0.0096	0.0223	3.5363	90.08
48105.10	−3.0883	−0.1238	0.0118	3.0908	91.15
48312.22	−2.6946	−0.1538	0.0096	2.6990	91.63
48323.18	−2.6012	−0.2592	0.0288	2.6141	92.85
48330.30	−2.6655	−0.3269	0.0080	2.6854	93.50
48344.19	−2.3786	−0.4399	0.0061	2.4190	95.24
48353.17	−2.0990	−0.3094	0.0093	2.1217	94.19
48386.14	−1.4219	−0.2747	0.0047	1.4482	95.47
48403.15	−1.2023	−0.2693	0.0071	1.2321	96.31
48414.14	−1.3156	−0.1031	0.0066	1.3196	92.24
48424.13	−1.4554	0.0781	0.0130	1.4575	88.46
48439.14	−2.3377	0.2418	0.0123	2.3502	87.05
48451.18	−2.6698	0.1469	0.0156	2.6738	88.43
48632.39	−2.5262	0.3261	0.0094	2.5472	86.32
48654.34	−3.8656	−0.1206	0.0356	3.8675	90.90
48660.38	−4.0641	−0.1378	0.0175	4.0664	90.97
48705.17	−3.4464	−0.8490	0.0091	3.5494	96.92
48717.17	−2.9896	−0.7952	0.0095	3.0935	97.45
48744.14	−2.1206	−0.3371	0.0125	2.1472	94.52
48760.13	−2.1241	−0.3186	0.0114	2.1478	94.27
48770.10	−2.0897	−0.4729	0.0083	2.1426	96.38
48794.17	−2.1481	−0.3708	0.0104	2.1798	94.90
48976.39	−1.0969	−0.4697	0.0078	1.1932	101.59
49036.23	−3.5427	−0.8853	0.0130	3.6516	97.02
49063.27	−4.6875	−0.9936	0.0137	4.7916	95.98
49098.14	−3.4049	−1.6164	0.0110	3.7691	102.70
49120.14	−2.0899	−1.0295	0.0110	2.3298	103.11
49361.46	−1.6281	−0.4091	0.0106	1.6787	97.05
49410.34	−3.7680	−0.7181	0.0120	3.8358	95.40
49442.19	−5.5675	−0.1014	0.0120	5.5685	90.52
49461.26	−4.2360	0.1133	0.0143	4.2375	89.23
49510.10	−2.3898	−0.7860	0.0200	2.5158	99.10
49708.30	−2.5568	−0.1917	0.0118	2.5640	92.14
49754.72	−3.1353	−0.9922	0.0182	3.2886	98.78
49793.70	−5.3530	−1.8564	0.0531	5.6658	99.56
49812.73	−6.4745	−2.4942	0.0144	6.9383	100.53
49856.65	−2.7648	−1.5222	0.0044	3.1561	104.42

[12] 5.3% of the original data is not included.

V Band Continued

MJD	Q(%)	U(%)	σ (%)	P(%)	PA(°)
49887.63	−2.5078	−1.0268	0.0109	2.7099	101.13
50123.89	−1.3096	−0.7078	0.0021	1.4886	104.20
50519.78	−1.9293	−1.3018	0.0069	2.3274	107.01
50553.71	−4.0460	−1.5934	0.0074	4.3484	100.75
50567.73	−3.8147	−1.2290	0.0071	4.0078	98.93
50594.68	−2.8819	−1.3238	0.0076	3.1714	102.34
50908.69	−2.4313	−2.2089	0.0067	3.2849	111.13
50922.60	−3.1733	−2.2177	0.0076	3.8715	107.47
51006.60	−1.3252	−1.0037	0.0056	1.6624	108.57
51161.94	−2.7787	0.0548	0.0113	2.7792	89.44
51175.94	−1.8002	−0.0521	0.0087	1.8010	90.83
51195.86	−1.5062	−0.6223	0.0132	1.6297	101.22
51223.84	−0.7813	−0.8250	0.0099	1.1363	113.28
51241.67	−0.4673	−0.7831	0.0042	0.9119	119.59
51564.89	−1.2816	−1.2390	0.0073	1.7826	112.02
51595.77	−1.6456	−1.2300	0.0104	2.0545	108.39
51615.78	−1.3106	−1.1283	0.0073	1.7294	110.36
51658.76	−0.6763	−0.6512	0.0075	0.9389	111.96
51685.70	−1.1735	−0.9872	0.0087	1.5336	110.04
51729.64	−1.2022	−0.2600	0.0248	1.2300	96.10
51731.69	0.3054	0.0961	0.0531	0.3202	8.73
51906.90	−2.0135	−0.5493	0.0117	2.0871	97.63
51920.93	−1.0365	−0.3383	0.0137	1.0903	99.04
51929.87	−0.8446	−0.3513	0.0106	0.9148	101.29
51961.92	−1.0843	−0.7491	0.0143	1.3179	107.32
51966.86	−1.0757	−0.9891	0.0214	1.4614	111.30
51972.67	−1.2595	−0.8579	0.0152	1.5240	107.13
52015.64	−0.7887	−0.3854	0.0098	0.8779	103.02
52041.66	−0.4622	−0.4771	0.0093	0.6643	112.95
52089.63	−0.9281	−0.7713	0.0118	1.2068	109.86
52319.86	−0.9375	−0.3709	0.0078	1.0082	100.79
52409.76	−0.4425	−0.6568	0.0078	0.7919	118.02
52432.63	−0.5149	−0.8935	0.0193	1.0313	120.02
52436.64	−0.7018	−1.0343	0.0272	1.2499	117.92
52856.58	−1.0210	−1.3093	0.0256	1.6603	116.03
53032.89	−0.9602	−0.7942	0.0186	1.2461	109.80
53051.93	−1.0078	−0.5898	0.0278	1.1676	105.17
53107.77	−0.7340	−0.6553	0.0101	0.9839	110.88
53128.68	−1.2203	−1.1517	0.0084	1.6779	111.67

B Band[13]

MJD	Q(%)	U(%)	σ (%)	P(%)	PA(°)
47596.22	−0.8930	−0.0751	0.0197	0.8961	92.41
47613.14	−0.7671	−0.0243	0.0387	0.7675	90.91
47897.38	−2.7158	−0.4892	0.0401	2.7595	95.11
47898.38	−2.6913	−0.3923	0.0187	2.7197	94.15
47920.30	−3.4709	−0.8812	0.0120	3.5810	97.12
47928.34	−3.1302	−0.9459	0.0171	3.2700	98.41
47951.17	−2.3054	−0.2855	0.0087	2.3230	93.53
47977.22	−1.7270	0.2222	0.0104	1.7412	86.33
47985.14	−1.5309	0.1032	0.0309	1.5344	88.07
47986.10	−1.6082	0.0480	0.0461	1.6089	89.15
47997.10	−1.2607	−0.1876	0.0087	1.2745	94.23
48047.13	−2.2950	−0.9577	0.0256	2.4868	101.33
48085.10	−5.1807	−0.3545	0.0285	5.1928	91.96
48091.11	−4.7352	−0.4013	0.0539	4.7521	92.42
48105.10	−3.8574	−0.7171	0.0249	3.9235	95.27
48312.22	−3.4526	−0.8701	0.0277	3.5605	97.07
48323.18	−3.3447	−1.0410	0.0773	3.5029	98.64
48330.30	−3.1172	−0.8659	0.0134	3.2353	97.76
48344.19	−2.7112	−0.9094	0.0119	2.8596	99.27
48353.17	−2.4815	−0.6872	0.0168	2.5749	97.74
48386.14	−1.7858	−0.6077	0.0103	1.8864	99.40
48403.15	−1.6152	−0.6655	0.0163	1.7469	101.20
48414.14	−1.8431	−0.3750	0.0137	1.8809	95.75
48424.13	−2.0846	−0.0048	0.0405	2.0846	90.07
48439.14	−3.5098	0.2352	0.0355	3.5177	88.08
48451.18	−3.9765	0.2246	0.0415	3.9829	88.38
48632.39	−3.9106	0.0672	0.0209	3.9112	89.51
48654.34	−6.1565	−0.3981	0.0749	6.1694	91.85
48660.38	−6.3311	−0.2739	0.0478	6.3370	91.24
48705.17	−4.2462	−2.1822	0.0185	4.7741	103.60
48717.17	−3.4880	−1.6922	0.0187	3.8768	102.94
48744.14	−2.6643	−0.2858	0.0306	2.6795	93.06
48760.13	−2.6508	−0.5168	0.0237	2.7008	95.52
48770.10	−2.7168	−0.7171	0.0170	2.8098	97.39
48794.17	−2.9581	−0.8292	0.0205	3.0721	97.83
48976.39	−1.6232	−0.8729	0.0157	1.8431	104.14
49036.23	−5.3916	−1.3073	0.0277	5.5478	96.82
49063.27	−6.7417	−2.5940	0.0289	7.2235	100.52
49098.14	−3.4938	−2.5955	0.0193	4.3523	108.30
49120.14	−2.1722	−1.4713	0.0208	2.6235	107.06
49361.46	−1.9103	−0.4595	0.0198	1.9648	96.76
49410.34	−5.0219	−1.4461	0.0190	5.2259	98.03
49442.19	−7.0680	−0.0130	0.0211	7.0680	90.05
49461.26	−4.8689	−0.4013	0.0238	4.8854	92.36
49510.10	−2.5215	−1.3621	0.0341	2.8659	104.19
49708.30	−2.6038	−0.2052	0.0224	2.6119	92.25
49754.72	−2.1451	−0.4287	0.1861	2.1876	95.65
49793.70	−4.7390	−2.0446	0.3496	5.1613	101.67
49812.73	−6.7010	−3.0553	0.1198	7.3646	102.26
49856.65	−2.6822	−1.9616	0.0160	3.3229	108.09
49887.63	−2.0118	−0.5950	0.0914	2.0980	98.24
50123.89	−1.5779	−1.1291	0.0057	1.9403	107.80

[13] 8.5% of the original data is not included.

B Band Continued

MJD	Q(%)	U(%)	σ (%)	P(%)	PA(°)
50519.78	−2.0959	−1.4808	0.0280	2.5663	107.62
50553.71	−5.5754	−1.1399	0.0400	5.6907	95.78
50567.73	−4.6752	−0.6399	0.0436	4.7187	93.90
50594.68	−2.9284	−0.6017	0.0449	2.9896	95.81
50908.69	−2.7841	−2.9026	0.0412	4.0219	113.10
50922.60	−3.8133	−2.2370	0.0556	4.4211	105.20
51006.60	−1.1324	−1.3323	0.0358	1.7485	114.82
51161.94	−2.7826	1.2156	0.0747	3.0365	78.20
51175.94	−1.1934	0.5076	0.0457	1.2969	78.48
51195.86	−0.9847	−1.1232	0.0726	1.4938	114.38
51223.84	−0.5986	−1.0404	0.0621	1.2003	120.04
51241.67	−0.4549	−1.3299	0.0177	1.4055	125.56
51564.89	−0.7175	−2.1901	0.0410	2.3046	125.93
51595.77	−1.4250	−2.0486	0.1098	2.4955	117.59
51615.78	−1.4719	−1.8325	0.0444	2.3504	115.61
51658.76	−0.5761	−0.6155	0.0709	0.8430	113.45
51685.70	−0.7971	−1.1518	0.0924	1.4007	117.66
51729.64	−1.8855	1.0757	0.4220	2.1708	75.15
51906.90	−1.8088	−0.1382	0.1213	1.8141	92.18
51920.93	−1.0466	−0.4451	0.1597	1.1373	101.52
51929.87	−0.2670	−0.7064	0.0659	0.7552	124.65
51961.92	−0.8243	−1.9325	0.1076	2.1010	123.45
51966.86	−0.5176	−0.7084	0.1355	0.8773	116.92
51972.67	−0.6920	−0.3067	0.1162	0.7569	101.95
52015.64	−0.4596	−0.4194	0.0680	0.6222	111.19
52041.66	−0.2472	−0.1828	0.0827	0.3074	108.24
52089.63	−0.1786	−1.2264	0.1509	1.2393	130.86
52319.86	−0.8769	−0.4959	0.0508	1.0074	104.75
52409.76	0.2109	−0.8673	0.1461	0.8925	141.83
52432.63	1.0177	−0.2773	0.2096	1.0543	172.38
52436.64	−0.2034	−4.1105	0.4207	4.1155	133.58
52856.58	−1.3099	−4.3169	0.2732	4.5113	126.56
53107.77	−0.1501	−1.3169	0.1252	1.3254	131.75
53128.68	−0.2682	−2.4187	0.3654	2.4335	131.84

R Band[14]

MJD	Q(%)	U(%)	σ (%)	P(%)	PA(°)
47596.22	−1.0052	0.0038	0.0084	1.0052	89.89
47613.14	−0.7503	−0.0102	0.0145	0.7503	90.39
47897.38	−1.6846	−0.0720	0.0240	1.6862	91.22
47898.38	−1.6724	−0.1176	0.0109	1.6766	92.01
47920.30	−2.1729	−0.2611	0.0069	2.1885	93.43
47928.34	−2.0820	−0.3374	0.0106	2.1092	94.60
47951.17	−1.6640	−0.2222	0.0055	1.6788	93.80
47977.22	−1.1534	−0.0285	0.0069	1.1538	90.71
47985.14	−1.0555	0.0005	0.0174	1.0555	89.99
47986.10	−1.1259	0.0101	0.0210	1.1259	89.74
47997.10	−0.8563	−0.0387	0.0050	0.8572	91.29
48047.13	−1.3536	−0.4571	0.0128	1.4287	99.33
48085.10	−2.6217	0.0074	0.0134	2.6217	89.92
48091.11	−2.7062	−0.0467	0.0237	2.7066	90.50
48105.10	−2.3058	−0.1001	0.0115	2.3079	91.24
48312.22	−2.2360	−0.0986	0.0101	2.2382	91.26
48323.18	−2.2155	−0.2031	0.0319	2.2248	92.62
48330.30	−2.1330	−0.2191	0.0077	2.1442	92.93
48344.19	−1.9692	−0.3484	0.0065	1.9998	95.02
48353.17	−1.6968	−0.1777	0.0099	1.7060	92.99
48386.14	−1.2317	−0.1998	0.0050	1.2478	94.61
48403.15	−1.1794	−0.2141	0.0073	1.1987	95.14
48414.14	−1.2422	−0.1859	0.0069	1.2560	94.26
48424.13	−1.3596	−0.0322	0.0155	1.3600	90.68
48439.14	−1.7973	0.0199	0.0131	1.7974	89.68
48451.18	−2.1841	−0.0457	0.0143	2.1846	90.60
48632.39	−2.0707	0.0500	0.0093	2.0713	89.31
48654.34	−2.9039	−0.2710	0.0293	2.9165	92.67
48660.38	−2.9122	−0.2969	0.0160	2.9273	92.91
48705.17	−2.7714	−0.6141	0.0093	2.8386	96.25
48717.17	−2.4033	−0.5174	0.0095	2.4584	96.07
48744.14	−1.6231	−0.2829	0.0141	1.6476	94.94
48760.13	−1.6438	−0.2834	0.0131	1.6680	94.89
48770.10	−1.6268	−0.3966	0.0091	1.6744	96.85
48794.17	−1.7498	−0.2974	0.0105	1.7749	94.82
48976.39	−0.9585	−0.3398	0.0079	1.0170	99.76
49036.23	−2.4243	−0.7597	0.0110	2.5405	98.70
49063.27	−3.2976	−0.9664	0.0123	3.4363	98.17
49098.14	−2.6065	−1.1064	0.0115	2.8316	101.50
49120.14	−1.7031	−0.6000	0.0110	1.8057	99.70
49361.46	−1.3553	−0.3855	0.0109	1.4091	97.94
49410.34	−2.8595	−0.5782	0.0116	2.9174	95.72
49442.19	−3.9837	−0.3644	0.0129	4.0004	92.61
49461.26	−3.1177	−0.2641	0.0149	3.1289	92.42
49510.10	−1.9036	−0.4616	0.0242	1.9587	96.82
49708.30	−2.0835	−0.2928	0.0119	2.1039	94.00
49754.72	−2.3279	−0.9545	0.0179	2.5159	101.15
49793.70	−3.6690	−1.6405	0.0055	4.0191	102.04
49812.73	−3.9438	−1.9017	0.0051	4.3783	102.87
49856.65	−2.1884	−1.2368	0.0021	2.5137	104.74
49887.63	−1.9244	−0.8970	0.0031	2.1232	102.50
50123.89	−1.1156	−0.7202	0.0010	1.3278	106.42

[14] 4.3% of the original data is not included.

R Band Continued

MJD	Q(%)	U(%)	σ (%)	P(%)	PA(°)
50519.78	−1.4309	−1.0035	0.0030	1.7477	107.52
50549.69	−2.3101	−1.1539	0.0081	2.5823	103.27
50553.71	−2.4907	−1.2400	0.0027	2.7823	103.23
50567.73	−2.5758	−1.0787	0.0030	2.7925	101.36
50594.68	−2.0587	−1.2156	0.0034	2.3908	105.28
50908.69	−1.6642	−1.5082	0.0027	2.2459	111.09
50922.60	−1.9720	−1.6141	0.0030	2.5483	109.65
51006.60	−1.0150	−0.8340	0.0025	1.3137	109.71
51161.94	−1.8818	−0.4033	0.0038	1.9246	96.05
51175.94	−1.3759	−0.3251	0.0031	1.4138	96.65
51195.86	−1.1999	−0.5815	0.0046	1.3334	102.93
51223.84	−0.7429	−0.5845	0.0031	0.9453	109.10
51241.67	−0.5509	−0.5979	0.0020	0.8130	113.67
51542.99	−0.9198	−0.2283	0.0031	0.9477	96.97
51564.89	−1.0987	−0.8980	0.0032	1.4190	109.63
51595.77	−1.3010	−0.8062	0.0037	1.5305	105.89
51615.78	−1.1462	−0.8009	0.0030	1.3983	107.47
51658.76	−0.8008	−0.5832	0.0030	0.9907	108.03
51685.70	−0.9717	−0.8428	0.0034	1.2863	110.47
51701.63	−1.2738	−0.6461	0.0035	1.4283	103.45
51729.64	−1.0665	−0.4695	0.0049	1.1653	101.88
51906.90	−1.5321	−0.6175	0.0039	1.6519	100.98
51920.93	−0.9663	−0.4671	0.0045	1.0733	102.90
51961.92	−0.9896	−0.6077	0.0041	1.1613	105.78
51972.67	−1.0613	−0.6291	0.0049	1.2337	105.33
52015.64	−0.8170	−0.2896	0.0038	0.8668	99.76
52041.66	−0.5671	−0.3782	0.0037	0.6817	106.85
52089.63	−0.8141	−0.6386	0.0035	1.0346	109.06
52318.87	−0.8676	−0.4416	0.0033	0.9735	103.49
52319.86	−0.8845	−0.4277	0.0033	0.9824	102.90
52409.76	−0.5896	−0.4553	0.0032	0.7450	108.84
52432.63	−0.6708	−0.7063	0.0041	0.9741	113.24
52773.69	−1.0122	−0.2240	0.0069	1.0367	96.24
52856.58	−0.9285	−0.9957	0.0065	1.3615	113.50
53032.89	−0.8679	−0.5548	0.0072	1.0301	106.30
53051.93	−0.9712	−0.5110	0.0077	1.0974	103.88
53107.77	−0.7555	−0.5354	0.0039	0.9259	107.66
53128.68	−0.9879	−0.7026	0.0037	1.2122	107.71

I Band[15]

MJD	Q(%)	U(%)	σ (%)	P(%)	PA(°)
47596.22	−0.9070	0.0378	0.0144	0.9078	88.81
47613.14	−0.6291	−0.0303	0.0225	0.6298	91.38
47897.38	−1.9683	−0.2439	0.0617	1.9834	93.53
47898.38	−1.9201	−0.2442	0.0293	1.9356	93.62
47920.30	−2.3904	−0.4379	0.0193	2.4302	95.19
47928.34	−2.0291	−0.4055	0.0285	2.0692	95.65
47951.17	−1.6992	−0.2669	0.0140	1.7200	94.46
47977.22	−1.0708	−0.0169	0.0174	1.0709	90.45
47985.14	−1.0819	−0.0153	0.0425	1.0820	90.40
47986.10	−1.2867	0.0614	0.0565	1.2882	88.63
47997.10	−0.8611	0.0188	0.0138	0.8613	89.38
48047.13	−1.4336	−0.5590	0.0379	1.5387	100.65
48085.10	−2.9976	−0.1690	0.0372	3.0024	91.61
48091.11	−3.3147	−0.5082	0.0687	3.3534	94.36
48105.10	−2.3814	−0.1501	0.0321	2.3861	91.80
48312.22	−2.5423	−0.2521	0.0271	2.5547	92.83
48323.18	−2.6087	−0.3103	0.0738	2.6271	93.39
48330.30	−2.2285	−0.3720	0.0182	2.2593	94.74
48344.19	−2.0616	−0.4911	0.0172	2.1193	96.70
48353.17	−1.6839	−0.2018	0.0275	1.6960	93.42
48386.14	−1.2782	−0.4370	0.0137	1.3509	99.44
48403.15	−1.3492	−0.4737	0.0189	1.4299	99.67
48414.14	−1.4705	−0.4741	0.0172	1.5450	98.94
48424.13	−1.7959	−0.2543	0.0446	1.8138	94.03
48439.14	−1.9978	−0.2393	0.0387	2.0121	93.42
48451.18	−2.3998	−0.0797	0.0371	2.4012	90.95
48632.39	−2.3437	−0.1707	0.0225	2.3499	92.08
48654.34	−3.4315	−0.3274	0.0680	3.4471	92.73
48660.38	−3.2757	−0.4100	0.0384	3.3013	93.57
48705.17	−3.0996	−1.1686	0.0255	3.3126	100.33
48717.17	−2.6038	−0.8128	0.0241	2.7277	98.67
48744.14	−1.5417	−0.3151	0.0386	1.5735	95.78
48760.13	−1.4364	−0.3954	0.0361	1.4899	97.70
48770.10	−1.4752	−0.4198	0.0272	1.5337	97.94
48794.17	−1.8569	−0.4233	0.0268	1.9046	96.42
48976.39	−0.9571	−0.3291	0.0195	1.0121	99.49
49036.23	−2.3390	−1.1376	0.0269	2.6009	102.97
49063.27	−3.4611	−1.9362	0.0321	3.9659	104.61
49098.14	−2.1025	−1.4215	0.0327	2.5380	107.03
49120.14	−1.3715	−0.5569	0.0272	1.4802	101.05
49361.46	−1.3537	−0.3874	0.0261	1.4081	97.99
49410.34	−2.9726	−0.8160	0.0308	3.0826	97.67
49442.19	−3.9259	−0.6664	0.0322	3.9821	94.82
49461.26	−2.8206	−0.4473	0.0393	2.8559	94.51
49510.10	−1.5342	−0.3599	0.0667	1.5759	96.60
49708.30	−1.8824	−0.3769	0.0281	1.9197	95.66
49754.72	−1.7583	−0.8961	0.0065	1.9735	103.50
49793.70	−2.5474	−1.6786	0.0019	3.0507	106.69
49812.73	−2.6955	−1.8808	0.0025	3.2868	107.45
49856.65	−1.6216	−1.3363	0.0015	2.1013	109.75
49887.63	−1.5056	−0.9223	0.0019	1.7657	105.75
50123.89	−0.9277	−0.8862	0.0009	1.2829	111.84

[15] 4.3% of the original data is not included.

I Band Continued

MJD	Q(%)	U(%)	σ (%)	P(%)	PA(°)
50519.78	−1.0131	−0.8866	0.0023	1.3463	110.59
50549.69	−1.5734	−1.0497	0.0044	1.8914	106.86
50553.71	−1.6369	−1.0193	0.0020	1.9283	105.96
50567.73	−1.6468	−0.9037	0.0022	1.8785	104.38
50594.68	−1.3344	−1.0548	0.0026	1.7009	109.16
50908.69	−1.0637	−1.2601	0.0019	1.6491	114.92
50922.60	−1.2018	−1.2783	0.0021	1.7546	113.38
51006.60	−0.5830	−0.8100	0.0016	0.9980	117.13
51161.94	−1.0792	−0.4207	0.0023	1.1583	100.65
51175.94	−0.7552	−0.3874	0.0021	0.8488	103.58
51195.86	−0.6665	−0.5395	0.0028	0.8575	109.50
51223.84	−0.5055	−0.5707	0.0019	0.7624	114.23
51241.67	−0.3814	−0.6097	0.0015	0.7192	118.99
51542.99	−0.4465	−0.5293	0.0020	0.6925	114.93
51564.89	−0.6632	−0.9092	0.0022	1.1254	116.95
51595.77	−0.9517	−0.7611	0.0024	1.2186	109.33
51615.78	−0.8966	−0.7828	0.0020	1.1902	110.56
51658.76	−0.6624	−0.6462	0.0019	0.9254	112.15
51685.70	−0.7065	−0.8213	0.0022	1.0834	114.65
51701.63	−0.8454	−0.7213	0.0022	1.1113	110.24
51729.64	−0.5785	−0.5743	0.0026	0.8152	112.40
51906.90	−1.0815	−0.5564	0.0025	1.2163	103.61
51920.93	−0.7217	−0.4684	0.0029	0.8604	106.49
51961.92	−0.7000	−0.6593	0.0025	0.9616	111.64
51972.67	−0.7321	−0.6048	0.0028	0.9496	109.78
52015.64	−0.6672	−0.2251	0.0025	0.7041	99.32
52041.66	−0.5813	−0.3441	0.0024	0.6755	105.31
52089.63	−0.6125	−0.6666	0.0022	0.9053	113.71
52318.87	−0.7378	−0.4916	0.0022	0.8866	106.84
52319.86	−0.7360	−0.4761	0.0022	0.8766	106.45
52409.76	−0.5331	−0.3178	0.0021	0.6206	105.40
52432.63	−0.5729	−0.5779	0.0023	0.8137	112.63
52773.69	−0.9177	−0.2020	0.0039	0.9397	96.21
52856.58	−0.7641	−0.9570	0.0032	1.2246	115.70
53032.89	−0.7590	−0.5722	0.0039	0.9505	108.51
53051.93	−0.8177	−0.5609	0.0039	0.9916	107.22
53107.77	−0.6796	−0.5812	0.0024	0.8943	110.27
53128.68	−0.8393	−0.6100	0.0024	1.0376	108.00

Appendix B

Photopolarimetric Data

In addition to the data found in Appendix A, HPOL provides tables of photopolarimetric data as well. The pipeline reduced polarimetric spectra from HPOL are available in tabular form through NASA's Multimission Archive at STScI (MAST), which is current only to 1998 at the time of this writing. The data from these tables provides the flux with respect to the wavelength across the entire UBVRI spectrum.

Since values for flux are larger when the source is brightest, the data has been normalized by integration order to preserve the changes in flux that are intrinsic to the source. Each curve represents a different observation. Different filters were also used, which produced curves that are offset to the main group of observations.

Figure B.1 shows the normalized flux as a function of wavelength in o Ceti. Note the changes in flux near $\lambda = 7500$. A dramatized change in flux occurs at $\lambda = 10^4$ in Figure B.2, the figure for R Leo. Figure B.3 only shows the observations made on V CVn with a single filter. A yellow line and a blue line have been added. The yellow line highlights the observation when V CVn was the brightest, and the blue line highlights the observation made when V CVn was the dimmest.

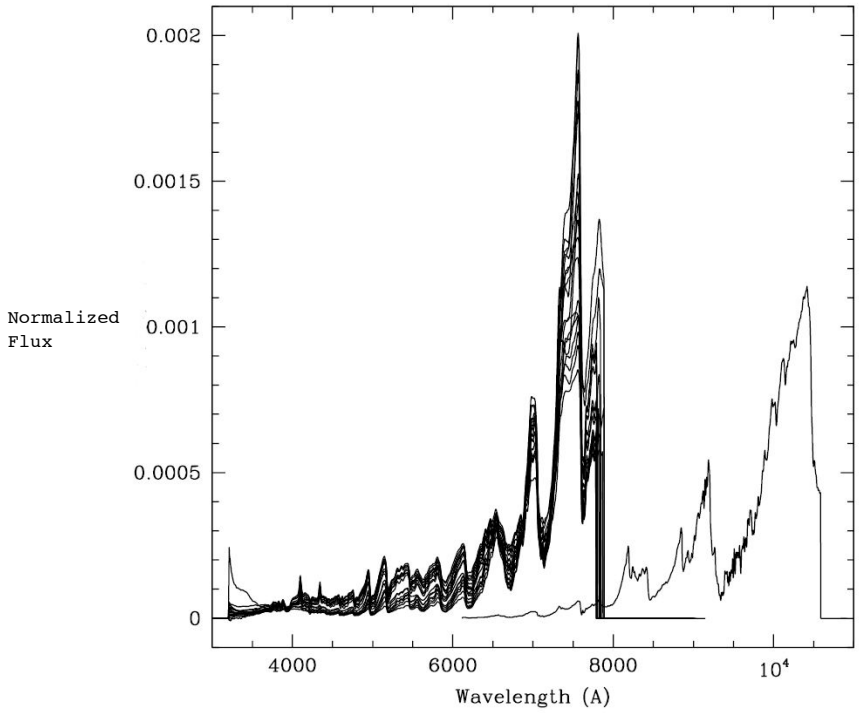

FIGURE B.1: HPOL-MAST Spectrophotometric data for Mira. Each curve represents the spectrophotometric readings from a single observation. The values for flux have been normalized with respect to the integral of the non-normalized curve with the largest values for flux.

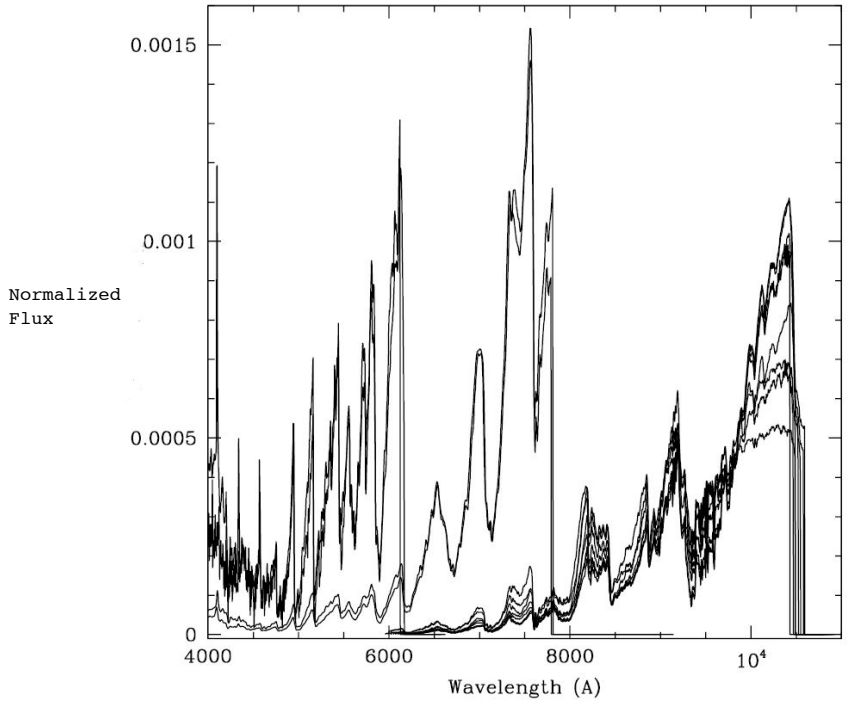

FIGURE B.2: HPOL-MAST Spectrophotometric data for R Leo. Each curve represents the spectrophotometric readings from a single observation. The values for flux have been normalized with respect to the integral of the non-normalized curve with the largest values for flux.

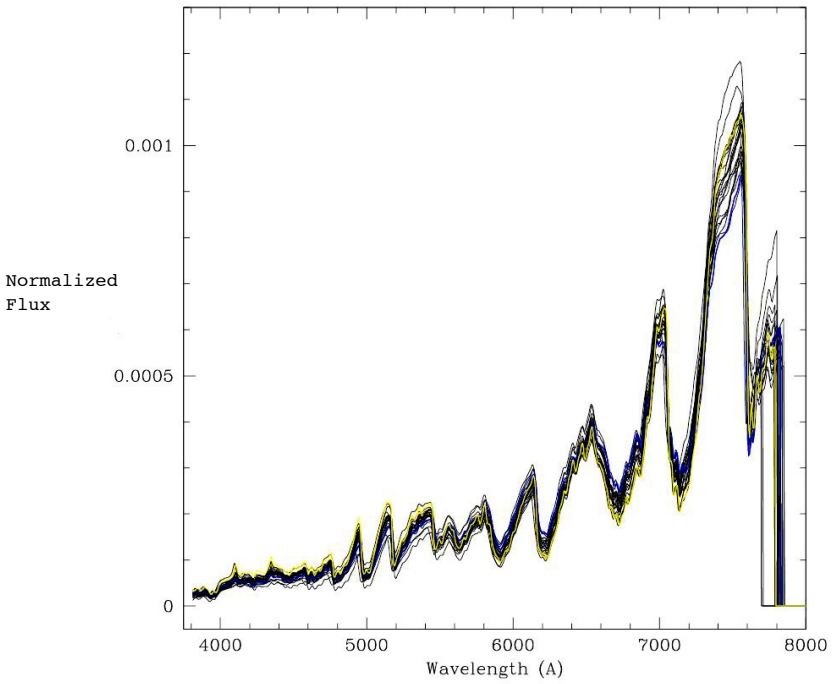

FIGURE B.3: HPOL-MAST Spectrophotometric data for V CVn. Each curve represents the spectrophotometric readings from a single observation. The values for flux have been normalized with respect to the integral of the non-normalized curve with the largest values for flux. The yellow curve represents the brightest observation of V CVn and the blue curve represents the dimmest observation of V CVn.

Bibliography

Al-Malki, M. B., Simmons, J. F. L., Ignace, R., Brown, J. C., Clarke, D., 1999, A&A 347, 919

Beiging, J. H., Schmidt, G. D., Smith, P. S., Oppenhiemer, B. D., 2006, AJ, 639, 1053-1068

Brown, J. C., & McLean, I. S., 1977, A&A, 57, 141-149

Clarke, D., 2010, Stellar Polarimetry, Weinheim: Wiley-VCH

Dyck, H. M., 1968, AJ, 688-696, 316

Fabas, N., Bèbre A., & Gillet D., 2011, AIP Conf. Proc., 215

Harrington, J. P., 1969, Ap. J, 3, 165

Hayes, D. P., & Russo, R. A., 1981, Inf. Bull. Var. Stars, 1910, 1, 2

Howk, J. C., & Savage, B. D., 1999, AJ, 117, 2077

Luttermoser, D. G., 2006, ASP Conf., 412, 243

Magalhaes, A. M., Coyne, G. V., Benedetti, E. K., 1986, AJ, 91, 919-924

Malatesta, K., 2006, AAVSO Website

Mattei, J. A., 1997, JAAVSO, 25, 57

McLean, I. S., Coyne, G. V., 1978, Ap. J, 226, L145-L148

Merrill, P. W., 1940, Univ. of Chicago Press

Neilson, R. H., Adams, A. M., Ignace, R., 2013, Pending Publication

Poliakova, T. A., 1989, A.O., Trudy, 42, 88-103

Raveendran, A. V., 2002, MNRAS, 336, 997

Serkowski, K., & Shawl, S. J., 2001, Ap. J, 122, 2017-2041

St-Louis, N., Chevrotière, A., & Moffat, A., 2011, AIP Conf. Proc., 1429, 176

Tomaszewski, L., Landstreet, J. D., McLean, I. S. et al., 1980, Ap. J, 238, 935-940

Uttenthaler, S., et al., 2011, A&A, 531A, 88U

Vink, S. V., 2011, AIP Conf. Proc., 1429, 148

Willson, L. A., 1976, ApJ, 205, 172

Willson, L. A., 2006, JAAVSO, 35, 65

Willson, L. A., Wallerstein, G., & Pilachowski, C. A. 1982, MNRAS, 198, 483

Yudin, R. V., & Evans, A., 2002, A&A, 386, 916